IRIS AperTO

UNIVERSITÀ DEGLI STUDI DI TORINO

AperTO - Archivio Istituzionale Open Access dell'Università di Torino

Impaired chromaffin cell excitability and exocytosis in autistic Timothy syndrome TS2-neo mouse rescued by L-type calcium channel blockers

This is the author's manuscript

Original Citation:

Availability:

This version is available http://hdl.handle.net/2318/1694883 since 2022-01-25T18:28:03Z

Published version:

DOI:10.1113/JP277487

Terms of use:

Open Access

Anyone can freely access the full text of works made available as "Open Access". Works made available under a Creative Commons license can be used according to the terms and conditions of said license. Use of all other works requires consent of the right holder (author or publisher) if not exempted from copyright protection by the applicable law.

(Article begins on next page)

16 August 2024

The Journal of Physiology

https://jp.msubmit.net

JP-RP-2018-277487X

Title: Impaired chromaffin cells excitability and exocytosis in autistic Timothy syndrome TS2-neo mouse rescued by L-type calcium channel blockers

Authors: Chiara Calorio
Daniela Gavello
Laura Guarina
Chiara Salio
Marco Sassoè-Pognetto
Chiara Riganti
Federico Bianchi
Nadja Hofer
Petronel Tuluc
Gerald Obermair
Paola Defilippi
Fiorella Balzac
Emilia Turco
Glenna Bett
Randall Rasmusson
Emilio Carbone

Author Conflict: No competing interests declared

Author Contribution: Chiara Calorio: Conception or design of the work; Acquisition or analysis or interpretation of data for the work; Drafting the work or revising it critically for important intellectual content; Final approval of the version to be published Daniela

Disclaimer: This is a confidential document.

Gavello: Acquisition or analysis or interpretation of data for the work; Drafting the work or revising it critically for important intellectual content; Final approval of the version to be published Laura Guarina: Acquisition or analysis or interpretation of data for the work; Final approval of the version to be published Chiara Salio: Acquisition or analysis or interpretation of data for the work; Final approval of the version to be published Marco Sassoè-Pognetto: Acquisition or analysis or interpretation of data for the work; Final approval of the version to be published Chiara Riganti: Acquisition or analysis or interpretation of data for the work; Final approval of the version to be published Federico Bianchi: Acquisition or analysis or interpretation of data for the work; Final approval of the version to be published Nadja Hofer: Acquisition or analysis or interpretation of data for the work; Final approval of the version to be published Petronel Tuluc: Acquisition or analysis or interpretation of data for the work; Final approval of the version to be published Gerald Obermair: Acquisition or analysis or interpretation of data for the work; Drafting the work or revising it critically for important intellectual content; Final approval of the version to be published Paola Defilippi: Acquisition or analysis or interpretation of data for the work; Final approval of the version to be published Fiorella Balzac: Acquisition or analysis or interpretation of data for the work; Final approval of the version to be published Emilia Turco: Acquisition or analysis or interpretation of data for the work; Final approval of the version to be published Glenna Bett: Acquisition or analysis or interpretation of data for the work; Final approval of the version to be published Randall Rasmusson: Acquisition or analysis or interpretation of data for the work; Final approval of the version to be published Emilio Carbone: Conception or design of the work; Acquisition or analysis or interpretation of data for the work; Drafting the work or revising it critically for important intellectual content; Final approval of the version to be published

Running Title: Altered chromaffin cell function induced by Cav1.2 gating mutation

Dual Publication: I do not have any dual publication ... I just cannot click on the "no" bouton

Funding: Fondazione Telethon (Telethon Foundation): Emilio Carbone, grant # GGP15110; Austrian Science Fund (FWF): Gerald J. Obermair, grant # SFB F4415; Italian Cancer Research (AIRC): Paola Defilippi, grant # IG-20107

Disclaimer: This is a confidential document.

Impaired chromaffin cells excitability and exocytosis in autistic Timothy syndrome TS2-neo mouse rescued by L-type calcium channel blockers

Chiara Calorio[1#], Daniela Gavello[1#], Laura Guarina[1], Chiara Salio[5], Marco Sassoè-Pognetto[4], Chiara Riganti[6], Federico Tommaso Bianchi[3], Nadja T. Hofer[7], Petronel Tuluc[7], Gerald Obermair[8], Paola Defilippi[3], Fiorella Balzac[3], Emilia Turco[3], Glenna C. Bett[2], Randall L. Rasmusson[2], Emilio Carbone[1*]

[1] Dept. of Drug Science, N.I.S. Centre, University of Torino, Italy, [2] Dept. of Physiology & Biophysics, State University of New York, Buffalo (NY), USA, [3] Dept. of Molecular Biotechnology and Health Sciences, University of Torino, Italy, [4] Dept. of Neuroscience Rita Levi Montalcini, University of Torino, Italy. [5] Dept. of Veterinary Sciences, University of Torino, Italy, [6] Dept. of Oncology, University of Torino, Italy, [7] Dept. of Pharmacology and Toxicology, Center for Molecular Biosciences, University of Innsbruck, Austria, [8]Dept. of Physiology & Medical Physics, Medical University of Innsbruck, Austria

Running title: Altered chromaffin cell function induced by Cav1.2 gating mutation

Keywords: Cav1.2 calcium channels, Nav sodium channels, burst firing, catecholamine secretion

[#] These authors contributed equally to the work

* *Corresponding author:* Emilio Carbone
Department of Drug Science
Corso Raffaello 30
10125 - Torino, Italy
e-mail: emilio.carbone@unito.it

Key points summary

- Tymothy syndrome (TS) is a multisystem disorder featuring cardiac arrhythmias, autism and adrenal gland dysfunction that originates from a *de-novo* point-mutation in the gene encoding Cav1.2 (*CACNA1C*) L-type channel.
- To study the role of Cav1.2 channel signals on autism, the autistic TS2-neo mouse has been generated bearing the G406R point-mutation associated with TS type-2.
- Using heterozygous TS2-neo mice, we report that the G406R mutation reduces the rate of inactivation and shifts leftward the activation and inactivation of L-type channels, causing marked increase of resting Ca^{2+}-influx ("window" Ca^{2+}-current).
- The increased "window current" causes marked reduction of Na_V channel-density, switches normal tonic firing in abnormal burst firing, reduces mitochondria metabolism, induces cell swelling and decreases catecholamine release.
- Overnight incubations with nifedipine rescue Na_V channel-density, the normal firing and the quantity of catecholamine released. We provide evidence that chromaffin cells malfunction derives from altered Cav1.2 channel-gatings.

Abstract

L-type voltage-gated calcium channels (Cav1) have a key role in long-term synaptic plasticity, sensory transduction, muscle contraction and hormone release. A point mutation in the gene encoding Cav1.2 (*CACNA1C*) causes Timothy syndrome (TS), a multisystem disorder featuring cardiac arrhythmias, autism spectrum disorder (ASD) and adrenal gland dysfunction. In the more severe type-2 form (TS2), the missense mutation G406R is on exon 8 coding for the IS6-helix of Cav1.2 channel. The mutation causes reduced inactivation and induces autism. How this occurs and how Cav1.2 gating-changes alter cell excitability, neuronal firing and hormone release on molecular basis is still widely unknown.

Here, using the TS2-neo mouse model of Timothy syndrome we show that the G406R mutation alters excitability and reduces secretory activity in adrenal chromaffin cells (CCs). Specifically, the TS2-mutation reduces the rate of voltage-dependent inactivation and shifts leftward the activation and steady-state inactivation of L-type channels. This markedly increases the resting "window" Ca^{2+} current that causes an increased percentage of CCs undergoing abnormal action potential (AP) burst firing, cell swelling, reduced mitochondrial metabolism and decreased catecholamine release. The increased "window Ca^{2+}-current" causes also decreased Na_V channel-density and increased steady-state inactivation that contribute to the increased abnormal burst firing. Overnight incubation with the L-type channel blocker nifedipine rescues the normal AP firing of CCs, the density of functioning Na_V channels and their steady-state inactivation. We provide evidence that CCs malfunction derives from the altered Cav1.2 channel gating and that dihydropyridines are potential therapeutics for ASD.

Introduction

Timothy syndrome (TS) is a rare multiorgan channelopathy characterized by cardiac arrhythmias, long QTs, immune deficiencies and autism (Splawski *et al.*, 2004; Splawski *et al.*, 2005). TS is associated with a *de novo* single point mutation in the pore-forming subunit of $Ca_V1.2$ L-type Ca^{2+} channels (*CACNA1C*) and occurs in two major forms (TS1 and TS2), depending on whether the point mutation appears on exon 8a (Splawski *et al.*, 2004) or exon 8 (Splawski *et al.*, 2005). The two exons code for the IS6 helix of $Ca_V1.2$ channel controlling the voltage-dependence of activation and inactivation. In the TS2 type, the mutation occurs either at gly406 (G406R) or gly402 (G402S) within exon 8 that is highly expressed in brain and heart (80%) and to a lesser extent in the adrenal glands (Splawski *et al.*, 2005). Both mutations cause reduced channel inactivation and increased Ca^{2+} influx during cell activity. Curiously enough, TS2 patients present autistic forms of behavior if they carry the G406R mutation but are neurologically intact if they exhibit the G402S mutation (Splawski *et al.*, 2005; Frohler *et al.*, 2014; Hiippala *et al.*, 2015). Recent findings suggest that the ability of the G406R vs. G402S mutation in inducing neurological abnormalities (Li *et al.*, 2016) is linked to the opposing effects of G406R and G402S mutations on $Ca_V1.2$ channel activation. The mutation G406R shifts the voltage-dependence of activation toward more negative potentials, whereas G402R shifts the activation to the opposite direction (Raybaud *et al.*, 2006; Dick *et al.*, 2016). A marked negative shift of V-dependent activation is also characteristic of the point mutations of the $Ca_V1.3$ α-subunit (A749G, V401L) identified in patients with autism spectrum disorder (ASD) (Pinggera *et al.*, 2015; Pinggera *et al.*, 2017).

TS is one of the most penetrant monogenic forms of autism and is widely studied either using cell transfection systems (Splawski *et al.*, 2004; Erxleben *et al.*, 2006; Barrett & Tsien, 2008; Yarotskyy *et al.*, 2008; Bidaud & Lory, 2011; Dick *et al.*, 2016) or somatic cell reprogramming to generate induced pluripotent stem cells (iPSCs) from patients with TS (Pasca *et al.*, 2011; Krey *et al.*, 2013). An alternative approach is now provided by the availability of the TS2-neo mouse, which exhibits behavioral traits reminiscent of ASD (Bader *et al.*, 2011; Bett *et al.*, 2012; Barnabei *et al.*, 2014). The TS2-neo mice have largely normal brain size and structure (Bader *et al.*, 2011). Their cortical neurons, however, exhibit the same activity-dependent dendritic retraction observed in rat cortical neurons transfected with Cav1.2 G406R-mutated channels and in human iPSC-derived neurons from individuals with TS (Krey *et al.*, 2013). The TS2-neo

mouse also displays altered brain activities that are common across several ASD mouse models (Ehlinger & Commons, 2017), and thus appears to be an interesting animal model for studying the origins of neuronal firing and Ca^{2+} signals mistuning that generate ASD.

Adrenal chromaffin cells (CCs) express high densities of Cav1.2 and Cav1.3 channels (Baldelli *et al.*, 2004; Marcantoni *et al.*, 2007; Marcantoni *et al.*, 2010) and are thus an excellent cell model to study the role of Cav1.2 channels on action potential (AP) firing and catecholamine secretion (Carabelli *et al.*, 2003; Lingle *et al.*, 2018). Here, we studied how the TS2-neo mutation alters mouse chromaffin cell (MCC) function. Our interest was further boosted by a recent case report of a 2 months-old TS patient, whose post-mortem autopsy revealed severe bilateral adrenal glands dystrophy, most likely caused by the increased intracellular Ca^{2+} associated with the Cav1.2 channel mutation that occurred mainly in the medulla (Kawaida *et al.*, 2016).

We found that TS2-neo MCCs possess L-type currents similar to the G406R-mutated phenotype described in transfected HEK cells having slower inactivation, leftward shifted voltage-dependent activation and inactivation and large "window" current at rest. The latter is likely the cause of the increased resting Ca^{2+} that switches AP firing from tonic to bursts, alters cell morphology and reduces mitochondrial metabolism and catecholamine secretion. High-resolution electron microscopy in intact adrenal glands of TS2-neo mice reveals extended cytoplasmic vacuolization and cell swelling that partly explains the reduced density of Na_V channels responsible for the altered AP firing. Overnight incubation of TS2-neo MCCs with sub-micromolar concentrations of the L-type channel blocker nifedipine (0.3 µM) effectively rescues the Nav channel density, the spontaneous firing and the secretory activity of TS2-mutated MCCs. Control tests indicate that chronic applications of 0.3 µM nifedipine are not *per se* beneficial on WT MCCs. On the contrary, the dihydropyridine (DHP) suppresses the resting spontaneous firing of WT cells. Our data provide evidence that the TS2-neo mouse is a valid murine model for studying the effects of the Cav1.2 G406R mutation on AP firing and Ca^{2+} signals associated with ASD.

Materials and Methods

Ethical approval – Ethical approval was obtained for all experimental protocols from the University of Torino Animal Care and Use Committee, Torino, Italy. All experiments were

conducted in accordance with the National Guide for the Care and Use of Laboratory Animals adopted by the Italian Ministry of Health. Every effort was made to minimize animal suffering and the number of animals used. For removal of tissues, animals were deeply anaesthetized with CO_2 inhalation and rapidly killed by cervical dislocation.

Cell culture – Chromaffin cells were obtained from male C57BL/6J mice (Envigo, San Pietro al Natisone, Italy) of 2 months. Under sterile conditions the abdomen was opened, the adrenal glands were isolated, and transferred to an ice cold Ca^{2+} and Mg^{2+} free Locke's buffer containing (in mM) 154 NaCl, 3.6 KCl, 5.6 $NaHCO_3$, 5.6 glucose and 10 HEPES, pH 7.4(Marcantoni *et al.*, 2009; Vandael *et al.*, 2012). Under a dissecting microscope the adrenal glands were decapsulated and subsequently subjected to an enzymatic dissociation with 20-25 units/ml papain (Worthington Biochemical Corporation, Segrate, Italy) dissolved in DMEM (GIBCO, Invitrogen Life Technologies, Monza, Italy) supplemented with 1.5 mM of L-cysteine, 1 mM of $CaCl_2$ and 0.5 mM of EDTA (Sigma Aldrich, Munich, Germany) for 25-30 minutes at 37°C in a water saturated atmosphere with 5% CO_2. Afterwards, two washing steps were performed with DMEM supplemented with 1mM $CaCl_2$ and 10 mg/ml of BSA (Sigma Aldrich). Adrenal medullas were re-suspended in DMEM containing 1% pen/strep and 15% fetal bovine serum (both from Sigma Aldrich) and were mechanically dissociated with a fire polished Pasteur pipette. A drop (100 µL) of this concentrated cell suspension was plated on poly-ornithine (1mg/ml) and laminin (5 µg/ml) coated Petri dishes and subsequently (30 minutes later) 1.9 ml of DMEM containing 1% pen/strep and 15% fetal bovine serum (all from Sigma Aldrich) was added. The primary chromaffin cell cultures were kept in an incubator at 37°C at water saturated atmosphere with 5% CO_2. Measurements were performed on cultured MCCs two to five days after plating.

Mouse genotyping – Genomic DNA extraction from mouse tail tissue was performed by incubating samples in 0.1 mg/ml proteinase K at 65°C for 3h. Samples were placed at 95°C for 10 minutes, centrifuged for 5 minutes at maximum speed, and 1 µl of the supernatant was used for PCR amplification. Primers specific for Cav1.2 (sense: 5'-*CCT CCA CTT TGC TTG TTC*-3'; anti-sense: 5'-*GGC TCC TGA GTG ACC CT*-3') were used to amplify a 667 bp fragment. Primer specific for the neomycin gene (5'-*GCT CCA GAC TGC CTT GGG AA*-3') was included in the reaction to amplify a 400 bp specific of the transgene. PCR conditions were as follows: denaturation at 94°C for 5 min followed by 35 cycles of 94°C for 30 s, annealing at 60°C for 30 s and extension at 72°C for 1 min, followed by a final extension at 72°C for 5 min. PCR products were separated by

agarose gel electrophoresis using 1% agarose and then visualized by CYBR Safe DNA gel staining for typing analysis. 1 Kb Plus DNA Ladder (Invitrogen) was used.

RNA isolation from tissue and cDNA synthesis – Adrenal glands were removed and transferred to an ice cold Ca^{2+}-and Mg^{2+}-free Locke's buffer containing (in mM): 154 NaCl, 3.6 KCl, 5.6 NaHCO3, 5.6 glucose, and 10 HEPES, pH 7.4. The glands were decapsulated and medullae were separated from the cortical tissue. Isolated medullae were immediately transferred into RNAlater RNA Stabilization Reagent (Qiagen, GmbH, Hilden, Germany). Purification of total RNA from adrenal medullae was implemented using Qiagen RNeasy mini kit (Qiagen, GmbH, Hilden, Germany) according to manufacturer's instructions. The RNA concentration was measured photometrically yielding approximately 40 ng/µl RNA.13 µl of total RNA was reverse transcribed using Maxima H Minus First Strand cDNA Synthesis kit with random hexamer primers (Thermo Fisher Scientific, Waltham, MA, USA).

Quantitative real-time PCR (qRT-PCR) – Custom TaqMan gene expression assays (Table 1) (Applied Biosystems, Foster City, CA, USA) were designed to span exon-exon boundaries.The expression of Cav1.2 exon 8 and exon 8a was assessed using a standard curve method based on PCR fragments of known concentration (Schlick *et al.*, 2010). Cav1.2 cDNA fragments were amplified from mouse whole brain or adrenal medulla using primers spanning exon 7-9 and specific for either exon 8 or exon 8a (Table 2).

The fragments were subsequently cloned into the pGFP37 vector. In order to generate DNA templates of known concentrations for qRT-PCR standard curves the concentration of the digested fragments was determined using the Quant-IT PicoGreen dsDNA Assay Kit (Invitrogen, Carlsbad, CA, USA). Subsequently, standard curves were generated using a serial dilution ranging from 10^7 to 10^1 DNA molecules in water containing 1 µg/ml of poly-dC-DNA (Midland, TX, USA). qRT-PCRs of standard curves and samples were performed as described previously(Schlick *et al.*, 2010). Samples for qRT-PCR quantification (50 cycles) contained 20 ng of total RNA equivalent of cDNA, the respective TaqMan gene expression assay, and TaqMan Universal PCR Master Mix (Applied Biosystems). Specificity of the custom designed assays recognizing either exon 8 or 8a was confirmed using different DNA ratios of corresponding and mismatched Cav1.2 DNA fragments. Importantly, both assays recognized only the corresponding fragment even in the presence of a 10-fold higher concentration of the other splice variant fragment (Fig. 1a). qRT-PCR was performed in duplicates from at least four independent RNA preparations from two

(WT) and three (TS2) biological replicates. Samples without template and RNA samples without reverse transcription served as negative controls. The expression of seven different endogenous control genes (ACTB, B2M, GAPDH, HPRT1, TBP, TFRC and SDHA (Schlick *et al.*, 2010)) was routinely measured and used for data normalization as previously described(Vandesompele *et al.*, 2002) (Fig. 1b). Briefly, data were normalized to the two most stable endogenous control genes (GAPDH and ACTB) and normalized molecule numbers were calculated for each assay based on their respective standard curve. Analyses were performed using the 7500 Fast System (Applied Biosystems, Foster City, CA, USA). Statistical analysis was performed using one-way ANOVA followed by Holm-Sidak post-test.

Action potential and ion current recordings – Macroscopic whole-cell currents and APs were recorded in perforated-patch conditions using a multiclamp 700-B amplifier and pClamp 10.0 software (Molecular Devices, Sunnyvale, CA, USA) (Marcantoni *et al.*, 2010; Vandael *et al.*, 2012). Traces were sampled at 10 KHz using a Digidata 1440A acquisition interface (Molecular Devices, Sunnyvale, CA, USA) and filtered using a low-pass Bessel filter set at 1-2 KHz. Borosilicate glass pipettes (Kimble Chase life science, Vineland, NJ, USA) with a resistance of 2-3 MΩ were dipped in an Eppendorf tube containing intracellular solution before being back filled with the same solution containing 500 µg/ml of amphotericin B (Sigma Aldrich, Munich, Germany), dissolved in DMSO (Sigma Aldrich, Munich, Germany) (Cesetti *et al.*, 2003). Recordings were initiated after amphotericin B lowered the access resistance below 15 MΩ (5-10 min). Series resistance was compensated by 60-80% and monitored throughout the experiment. Fast capacitive transients during step-wise depolarizations (in voltage-clamp mode) were minimized online by the use of the patch clamp analogue compensation. Uncompensated capacitive currents were further reduced by subtracting the averaged currents in response to P/4 hyperpolarizing pulses.

The normalized voltage-dependent conductance of Cav channels (g_{Ca}), was calculated with the equation: $g_{Ca} = I_{Capeak} / (V - E_{Ca})$, with E_{Ca} equal to the reversal potential for Ca^{2+}, and fitted with a Boltzmann function with variable $V_{1/2}$ (in mV) and k slope (in mV) (Guarina *et al.*, 2017). The same was done for g_{Na} and g_{BK}.

Solutions – Intracellular solution for current-clamp and Na^+ and K^+ current measurements in voltage clamp or AP-clamp mode was composed of (in mM) 135 KAsp, 8 NaCl, 2 $MgCl_2$, 5 EGTA, 20 HEPES, pH 7.4 (with KOH; Sigma Aldrich). For Ca^{2+} current recordings the intracellular solution

contained (in mM) 135 Cs-$MeSO_3$, 8 NaCl, 2 $MgCl_2$, 5 EGTA and 20 HEPES, pHo 7,4 (with CsOH; Sigma Aldrich). The extracellular solution used for current-clamp measurements is a physiological Tyrode's solution containing in mM: 130 NaCl, 4 KCl, 2 $CaCl_2$, 2 $MgCl_2$, 10 glucose and 10 HEPES; pHo 7.4 (with NaOH; Sigma Aldrich). The same solution was used to measure K^+ currents. K_V currents were obtained by adding 1 µM paxilline to the external solution while Ca^{2+}-activated BK currents were estimated by subtracting K_V from the total K^+ currents. The extracellular solution used for Na^+ current measurements was composed of (in mM): 104 NaCl, 30 TEACl, 4 KCl, 2 $CaCl_2$, 2 $MgCl_2$, 10 glucose and 10 HEPES, pHo 7,4 (with NaOH). The extracellular solution used for Ca^{2+} and Ba^{2+} current measurements in voltage-clamp configuration contained (in mM): 135 TEACl, 10 $CaCl_2$ (or 10 $BaCl_2$), 2 $MgCl_2$, 10 glucose and 10 HEPES, pHo 7.4 (with TEA-OH; Sigma Aldrich). Nifedipine and verapamil were obtained from Sigma Aldrich. The two drugs were dissolved, stored and used as previously described (Marcantoni *et al.*, 2010).

Membrane capacitance changes to monitor vesicle secretion **–** Ca^{2+} currents and the corresponding depolarization-evoked capacitance changes were measured in the perforated-patch configuration using an EPC-10 double patch amplifier (HEKA Elektronic, Lambrecht, Germany) (Carabelli *et al.*, 2003; Carabelli *et al.*, 2007; Marcantoni *et al.*, 2009). Mouse chromaffin cells were kept in saline solution, containing (in mM): 4 TEACl, 126 NaCl, 10 $CaCl_2$, 4 KCl, 2 $MgCl_2$, 10 Glucose, 10 HEPES (pH 7.4 with NaOH). The internal solution contained in mM: 135 $CsMeSO_3$, 8 NaCl, 2 $MgCl_2$, 20 HEPES (pH 7.3 with CsOH) plus amphotericin B (Sigma). Ca^{2+} currents were evoked by applying step depolarizations (100 ms duration), from an holding potential of −70 mV to +10 mV. Superimposed on the square pulse, a sinusoidal wave function (1000 Hz, ± 25 mV) was applied in order to monitor membrane capacitance increases following the depolarizing step using the Lockin extension of the Patchmaster software. Fast capacitive transients due to depolarizing pulses were minimized online by the patch-clamp analog compensation. Series resistance was compensated by 80% and monitored during the experiment. The amount of Ca^{2+} entering the cells during a depolarization (quantity of charge in pC) was calculated as the time integral of the Ca^{2+} current. All the experiments were performed at room temperature. Ca^{2+} currents were sampled at 10 kHz and low-pass filtered at 2 kHz.

TEM imaging **–** Adrenal glands were freshly dissected from male C57BL/6J (n= 3) and TS2-neo mice (n= 3) and fixed by immersion in 4% formaldehyde + 2% glutaraldehyde in phosphate

buffer (PB, 0.1 M, pH7.4) overnight at 4°C. After washing in PB, the glands were post-fixed in osmium ferrocyanide (1 volume of 2% aqueous osmium tetroxide : 1 volume of 3% potassium ferrocyanide) for 1 hour at 4°C, dehydrated for 15 min in increasing concentrations of acetone (30%, 60%, 90%, 100%), and then embedded in Spurr resin in 0.5 ml Eppendorf tubes. Ultrathin sections were cut with an ultramicrotome (EM UC6, Leica), collected on uncoated nickel grids (200 mesh) and counterstained with lead citrate (10 min)(Salio *et al.*, 2017). Grids were observed with a JEM-1010 transmission electron microscope (Jeol, Japan) equipped with a side-mounted CCD camera (Mega View III, Olympus Soft Imaging System, Germany). To determine the area of the cell profiles visible in single sections, fifty MCCs (6000x magnification) from both C57BL/6J and TS2-neo mice were randomly selected. The surface of sectioned cells was measured by using the analySIS software (Olympus Soft Imaging System, Germany). The number of mitochondria/area (N/μm^2) and large dense-core granules/area (N/μm^2) were calculated in the same MCCs by using the count particle function of ImageJ software (NIH, Bethesda, MD) and results were expressed as mean ± SEM.

Mitochondrial respiration and ATP synthesis – The electron transport between complexes I and III was measured in mitochondrial extracts as described earlier (Campia *et al.*, 2009). The results were expressed as nmol reduced cytochrome c/min/mg mitochondrial proteins. The amount of ATP in mitochondria was measured with the ATP Bioluminescent Assay Kit (FL-AA, Sigma), using a Synergy HT Multi-Mode Microplate Reader (Bio-Tek). ATP was quantified as relative light units (RLU); data were converted into nmol ATP/mg mitochondrial proteins.

Mitochondrial electric potential (Δψ) measurement – The mitochondrial electric potential (Δψ) was measured using the JC-1 staining method (Riganti *et al.*, 2015). 1 × 106 cells, re-suspended in 0.5 mL PBS, were incubated for 30 min at 37 °C with 2 µmol/L of the fluorescent probe JC-1 (Biotium Inc., Hayward, CA), then centrifuged at 13,000 × g for 5 min and re-suspended in 0.5 mL PBS. The fluorescence of each sample was read using a Synergy HT Multi-Mode Microplate Reader (BioTek): the red fluorescence, index of polarized mitochondria, was detected at 550 nm (λ excitation) and 600 nm (λ emission); the green fluorescence, index of depolarized and damaged mitochondria, was detected at 485 nm (λ excitation) and 535 nm (λ emission). The fluorescence units were used to calculate the percentage of green-fluorescent (i.e. depolarized/damaged mitochondria) versus red-fluorescent mitochondria (i.e. polarized mitochondria).

DAPI and TUNEL immunofluorescence assays – Adrenal medulla glands were dissected and fixed for 12-16 h at 4°C, equilibrated in 30% sucrose in PBS for 12-24 h at 4°C, embedded with Tissue-TEK (O.C.T, Sakura Finetek, Alphen aan den Rijn, The Netherlands), frozen in liquid nitrogen and stored at -20°C as already detailed(Sgro *et al.*, 2016; Bianchi *et al.*, 2017). Sectioning was then performed with a cryostat (20 µm). For staining, cryo-sections were subjected to antigen retrieval using 10 mM Na Citrate pH 6.5, 1% Glycerol in PBS. Sections were then permeabilized with 0.3% Triton X-100 in PBS for 30 minutes (min) and quenched with 0.1 M glycine for 30 min. Apoptosis was analyzed by the TUNEL assay using "In Situ cell death detection kit, TMD red" (Roche, Basel; Switzerland) according to manufacturer's protocol. Following TUNEL staining, sections were counterstained with 4´,6- diamidino-2-phenylindole (DAPI) for 30 min at RT and sections were mounted using ProLong anti-fade reagent (Thermo Fisher Scientific, Waltham, MA, USA).

Microscopy and image analysis – Imaging was performed using a Leica TCS SP5-AOBS 5-channel confocal system (Leica Microsystems GmbH, Germany) equipped with a 405 nm diode, an argon ion, a 561 nm DPSS and a HeNe laser. Fixed slices were imaged using a PL APO 40x/1.2 NA oil immersion objective (Bianchi *et al.*, 2017). All the images were analyzed by using Fiji Software.

Statistics – Data are given as mean ± SEM for n number of cells. Statistical significance was estimated using either paired/unpaired Student t-tests or one-way ANOVA followed by a Holm-Sidak *post hoc* test in case of two or multiple groups of measurements had to be compared. Data were found statistically significant when $p \leq 0.05$. Statistical analysis was performed with either SPSS software (version 20.0, IBM) or Origin 8.5 (OriginLab Corporation, Northampton, MA, USA). Off-line data analysis was performed with pClamp 10.0 and Origin 8.5 software.

Results

qPCR analysis of Cav1.2 exon 8 and exon 8a expression in MCCs

Cav1.2 and Cav1.3 are the only L-type channels effectively expressed in MCCs (Baldelli *et al.*, 2004) with Cav1.2 contributing to nearly half of the L-type current (Marcantoni *et al.*, 2010). Nevertheless, it has never been tested how much of the Cav1.2 exon 8 or exon 8a splice variants is expressed in the MCCs of the adrenal medulla. Cav1.2 exons 8 and 8a are mutually exclusive exons, with high sequence similarity, encoding for the IS6 transmembrane domain (Fig. 2a,b). To

identify the amount of exon 8 and 8a splice variants expressed in the adrenal medulla of WT and heterozygote TS2-neo mice we performed a standard curve-based absolute qRT-PCR analysis (Schlick *et al.*, 2010). Fig. 2c shows that WT MCCs express exon 8 and exon 8a in a ratio of 1:5 (***p< 0.001), while the heterozygote TS2-neo MCCs express the two exons in a ratio of 1:1. The ~50% reduced expression of exon 8a in TS2-neo compared to WT MCCs (***p< 0.001) is attributed to the neo-cassette that introduces a stop codon in exon 8a of the mutated allele, thus likely rendering the truncated mRNA sensitive to nonsense mediated degradation. Interestingly, the total amount of Cav1.2 mRNA was similar in heterozygote TS2 and WT MCCs confirming a previously suggested upregulation of exon 8 as a consequence of the reduced expression of exon 8a (***p< 0.001) (Bader *et al.*, 2011). Our exon 8 qRT-PCR assay does not discriminate between WT and TS2-mutated allele and therefore we cannot exactly quantify the total amounts of WT and TS2-mutated exon 8. Given the unpredicted upregulation of exon 8 in TS2-neo adrenal medulla, it seemed reasonable to expect that the expression ratio of mutated vs. WT allele may vary between 1:1 and 1:5.

Altered L-type channel gating in TS2-neo MCCs

L-type currents were recorded in isolation by incubating MCCs in solutions containing 2 µM ω-CTx-MVIIC, 60 nM SNX-482 and 3 µM TTA-P2 to selectively block P/Q, N, R and T-type Ca^{2+} channels which are effectively expressed in MCCs (Mahapatra *et al.*, 2012). Pharmacologically isolated L-type currents were recorded in 10 mM Ca^{2+}. They activated around −40 mV, peaked at nearly +15 mV, reversed at around +60 mV (Fig. 3a,c) and were fully blocked by 15 µM nifedipine in WT MCCs (Fig. 3b, n= 6) (Marcantoni *et al.*, 2010). The corresponding normalized L-type channel conductance ($g_{Ca}(V)$) had half-maximum values ($V_{½}$) at −0.7 mV and steep voltage-dependence (k= 10.7 mV for an e-fold change; n= 17) (Fig. 3d). In TS2-neo MCCs, Ca^{2+} currents activated at slightly more negative potentials (Fig. 3a,c) and reached similar current amplitudes at +20 mV compared to WT MCCs (n= 17; Fig. 3e). The corresponding current-densities (pA/pF) were significantly smaller (mean current densities were 15.2 and 9.9 pA/pF WT vs. TS2-neo cells; Fig. 3e) due to the increased cell capacitance (Fig. 3e). The membrane capacitance increased by 31% in the cells used for Fig. 3c (n= 19 WT and n= 20 TS2-neo; *p< 0.05) but the increase was consistently observed over a wider pool of MCCs (n= 65 and n= 59 cells; 14.5%, *p< 0.05; Fig. 3e, middle). The negative voltage-shift of channel activation was quantified by comparing the $g_{Ca}(V)$

curve to WT cells. TS2-neo data were best fitted with a Boltzmann function shifted by ~−5 mV with respect to WT cells (Fig. 3d).

In 2 mM Ca^{2+} L-type Ca^{2+} currents in MCCs inactivate with fast and slow decaying components during long depolarizations, while in 2 mM Ba^{2+} only slow inactivation is observed. The fast component represents the Ca^{2+}-dependent inactivation (CDI) and slow component the voltage-dependent inactivation (VDI) (Scharinger *et al.*, 2015). In TS2-neo mice L-type channel inactivation is expected to be slower and less complete (Splawski *et al.*, 2005), but it is unclear whether the effect is preferentially on CDI or VDI (Barrett & Tsien, 2008; Dick *et al.*, 2016). Therefore, we compared the time course of L-type Ca^{2+} currents during pulses of 1 s to +10 mV in 10 mM Ca^{2+} in WT and TS2-mutated cells. In both cell types, L-type channel inactivation occurred to a variable degree but in all cells tested inactivation exhibited a fast and a slow component. The percentage of Ca^{2+} current inactivation after 1 s was significantly attenuated in TS2-neo MCCs (Fig. 4a). The remaining Ca^{2+} current after 1 s increased from 44 ± 3% (n= 11) in WT to 59 ± 3% (n= 11) in TS2-neo MCCs (**p< 0.01) preserving the characteristic double exponential decaying time course. Best fit of the mean normalized Ca^{2+} currents in WT and TS2-neo cells gave the following values for the amplitudes (A_{fast}, A_{slow}), time constants (τ_{fast}, τ_{slow}) and baseline value (C) of the two exponentials: A_{fast} −0.15, τ_{fast} 37.9 ms; A_{slow} −0.55, τ_{slow} 851 ms, C −0.29 in WT (n= 11) and A_{fast} −0.14, τ_{fast} 34.5 ms; A_{slow} −0.38, τ_{slow} 727 ms, C −0.48 in TS2-neo (n =11). The mutation mainly reduced the size of A_{slow} (−0.55 vs. −0.38) associated with the VDI while preserves the size of A_{fast} and time constants of both components. This was confirmed by the changes of Ba^{2+} current inactivation. Ba^{2+} currents lack the fast CDI component in TS2-neo MCCs (Fig. 4b). After 1 s, the persisting Ba^{2+} current is ~15% higher in TS2-mutated cells (*p< 0.05; Fig. 4b). Curve fitting furnishes the following amplitudes and time constants: A_{slow} −0.67, τ_{slow} 1230 ms, C = −0.23 in WT and A_{slow} -0.59, τ_{slow} 1280 ms, C −0.41 in TS2-neo cells, suggesting that the mutation mainly decreased the size of A_{slow} by ~14% by an increased percentage of non-inactivated current. We also quantified the voltage-dependence of CDI using a double pulse protocol (Fig. 4c). Inactivation revealed the typical U-shaped curve and was significantly different at more positive voltages (Fig. 4c) (Scharinger *et al.*, 2015).

Resting "window" Ca^{2+} current increases in TS2-neo MCCs

To quantify the resting window Ca^{2+} current we determined the voltage-dependence of steady-state inactivation (SSI) to estimate the availability of L-type channels at various potentials.

Fig.5a,b illustrate the pulse protocol used (Pinggera *et al.*, 2015; Pinggera *et al.*, 2017) and shows examples of Ca^{2+} currents recorded during test pulses P_1 and P_2 at +20 mV separated by 5 s depolarization to a pre-determined potential in WT (black traces) and TS2-neo MCCs (red traces). The ratio I_{P2}/I_{P1} gives the percentage of available L-type channels at the fixed potential. As for other slowly inactivating voltage-gated Ca^{2+} channels the I_{P2}/I_{P1} ratio is maximal at very negative voltages and decreases steeply in a voltage-dependent manner with increasing voltages to reach a minimum at positive potentials in WT MCCs (Fig. 5c). In TS2-neo MCCs, channel availability is shifted toward negative potentials in a broad range of voltages and exhibits an increased minimum (from 0.15 to 0.23) above 0 mV (Fig. 5c). Best fit analysis using the Boltzmann functions reveals a −9 mV shift of $V_{½}$ in TS2-neo cells.

The negative shifts of both SSI and activation predicted an increased window Ca^{2+} current (I_W) near resting potential. We calculated I_W by first multiplying the two curves to give the probability of open L-type channels ($p_o(V)$; Fig. 5d, *dotted curves*) and then multiplying for the driving force (V-E_{Ca}) to estimate the amount of normalized I_W in WT and TS2-neo cells (*continuous curves;* Fig. 5d-*bottom*). A drastic increase of inward Ca^{2+} currents was evident in mutated MCCs, particularly around resting voltages in 10 mM Ca^{2+} (−60 to −40 mV; *shadowed area*).

Spontaneous AP firing is altered in TS2-neo MCCs

A major consequence of the altered Cav1.2 activation/inactivation kinetics and increased window Ca^{2+} current in TS2-mutated MCCs is a drastic change in spontaneous AP firing at rest. The mutation had no effects on resting potential (−47.9 vs. −48.5 mV; Fig. 6a) but increased the percentage of cells that underwent burst firing (Fig.6b). Mutated and WT MCCs had similar percentage of silent cells (20% WT n= 20 total cells vs. 15% TS2-neo n= 20 total cells) but differing percentages of burst and tonic firing cells at rest. Half of TS2-neo cells underwent burst firing, while only 35% had tonic firing (Fig. 6b). In contrast, WT cells had mainly tonic firing (65%) while only 15% produced bursts (*p< 0.05; Chi-square test).

TS2-neo mutation changed also the waveform of single APs and bursts. Tonic firing (Fig. 6c,d), occurred at about the same frequency (0.9 vs. 1.1 Hz; Fig. 6c) but had significantly smaller amplitude (36.0 vs. 57.5 mV; **p< 0.01), larger half-width (10.2 vs. 3.9 ms; **p< 0.01), reduced after-hyperpolarization (−4.3 vs −7.2 mV; *p< 0.05) and slower rising phases (Fig. 6f). The rising phase velocity was estimated from the mean maximum of the *dV/dt* vs. *V* phase-plane plot of six

consecutive APs (14.6 vs. 48.5 V/s; **p< 0.01; Fig. 6g), suggesting a markedly reduced density of Nav channels that would be available to support AP upstroke.

The TS2-neo mutation altered also the waveform of bursts (Fig. 7a,b). Bursts in mutated cells had undershoot peaks (below zero). The amplitude of the first and last AP were significantly smaller than in WT MCCs (−15.6 and −24.9 mV in TS2-neo n= 7 vs. 5.0 and −16.3 mV in WT n= 4; **p< 0.01). We also noticed that burst firing occurred either at low (n= 4 out of 7 cells; Fig. 7b; slow burst) or at high frequency in which single spikes appeared intermixed with burst (n= 3 out of 7 cells; Fig. 7b; fast burst). The two types of firing were pooled together to determine the mean bursts duration, the mean plateau amplitudes and number of bursts per minute. These parameters were estimated as shown in the inset of Fig. 7a (red trace; see figure legend for details) and as previously described in Fig. 9 of Guarina et al., 2017. They were comparable to WT MCCs (Fig. 7d), while the mean number of events decreased significantly from 4.0 to 2.7 (**p< 0.01) (Fig. 7c), suggesting rapid loss of APs during the plateau depolarization of the burst. In conclusion, the TS2-neo mutation induces an increased percentage of MCCs undergoing bursts with APs of lower amplitudes that quickly decay during the plateau potential. Most likely, this is due to the reduced density of Nav channels that causes reduced activation of BK and K_V channels with consequent decrease of the repolarization phase and subsequent insufficient recovery of inactivated Nav channels able to sustain the following APs (see Vandael et al., 2015).

Nav1 channel density is markedly reduced in TS2-neo MCCs

The increased "window" Ca^{2+} current (Fig. 5d) and the drastic changes of AP firing in TS2-mutated MCCs (Fig. 6, 7) suggest that the Cav1.2 TS2-mutation may produce drastic changes to the ionic conductances responsible of MCCs excitability. We therefore tested whether the TS2-mutation altered the voltage-dependence and size of Nav currents responsible of AP upstroke (Vandael *et al.*, 2015b; Lingle *et al.*, 2018). We found that peak Nav currents during step depolarization to -10 or 0 mV in 2mM Ca^{2+} had variable amplitudes with a clear trend to decrease in TS2-mutated MCCs (mean values 12.5 vs. 9.4 nA in WT vs. TS2-neo cells) (Fig. 8a, b). The trend was converted into a significant decrease of Nav current density when normalized for the increased membrane capacitance (Fig. 8b-*middle*), in good agreement with the capacitance values of Fig. 3e. Nav current densities were ~43% smaller in TS2-neo MCCs (*p< 0.05; Fig. 8b-*right*).

The shape of the normalized *I-V* curves and the voltage-dependence of Nav channel conductance, $g_{Na}(V)$, were not significantly affected (Fig. 8c, d) and no changes were observed in the voltage-dependence of fast inactivation (Fig. 8e), suggesting that the Cav1.2 mutation has no major effects on the activation-inactivation kinetics of functionally expressed Nav channels. The 43% decrease of Nav current density resulted from a decreased number of functional Nav channels and an increased size of cell area (swelling), most likely associated with the altered resting Ca^{2+} level induced by the increased "window" Ca^{2+} current.

Since increases of intracellular Ca^{2+} are likely to alter a variety of intracellular pathways that regulate the SSI of Nav channel (Carr *et al.*, 2003; Jo & Bean, 2017), we also tested whether the voltage-dependence of the slow recovery from inactivation of these channels was altered. Fig. 8f shows that indeed Nav channels of mutated MCCs recover less during 5 s long pulses more positive than −40 mV. The SSI curve had more or less the same $V_{1/2}$ voltage (-30 mV, WT n= 11 vs. -28 mV TS2-neo n= 14) but was significantly lower at potentials > −40 mV. Minimum values for SSI at +30 mV were 0.57 for WT and 0.43 for TS2-neo cells, suggesting a reduced number of available channels at potentials more positive than -40 mV. This explains why during prolonged depolarization between −40 and −20 mV (Fig. 7b,c) a considerable fraction of Na_V channels remains inactivated and do not participate to the burst firing in mutated MCCs.

BK channel currents are preserved in TS2-neo MCC

Given the importance of BK channels in the control of AP repolarization and setting of burst firing in MCCs (Marcantoni *et al.*, 2010; Martinez-Espinosa *et al.*, 2014; Lingle *et al.*, 2018) we checked whether BK currents were altered by the TS2-neo mutation. The voltage-dependence of BK channels was tested using the pulse protocol shown in Fig. 9a (Gavello *et al.*, 2015; Guarina *et al.*, 2017). BK currents were obtained by first determining the contribution of K_V currents to the total by adding 1 µM paxilline to block BK channels (Zhou & Lingle, 2014). Subtraction of Kv currents from the total gave the BK currents (bottom panel). Despite a sizeable $V_{1/2}$ leftward shift, the voltage-dependence of BK channels in TS2-mutated cells (n= 10) was not significantly different from WT MCCs (n= 8) (Fig. 9b).

We also tested the Ca^{2+}-dependence of BK channels by preloading the cell with Ca^{2+} using pre-steps of increasing voltage (-60 to +120 mV) to activate BK and K_V channels and measure their peak current amplitude at +120 mV. Since at +120 mV there is no inward Ca^{2+}-entry, the outward current is the K_V current (I_{Kv}). This, subtracted from the total current gives I_{BK} (arrows in

Fig. 9c-*right*). In mutated MCCs (n= 8) both the maximal peak amplitude at +20 mV (2.3 ± 0.8 nA) and the voltage-dependence of the "bell shaped" I-V relationship of BK channels were no significantly different from WT-MCCs (n= 10) (Fig. 9d, e). Similar maximal amplitudes in WT and TS2-neo cells were also found for I_{Kv} at +120 mV (Fig. 9e). We also found no statistically significant changes in the time course of BK current inactivation (whether inactivating or noninactivating, (Solaro *et al.*, 1995)) between WT and TS2-neo MCCs. In n= 10 TS2-neo mutated cells 6 where noninactivating and 4 inactivating while in n= 8 WT cells 4 were inactivating and 4 noninactivating (chi-square test, p= 0.67). The same ratio of activating vs. noninactivating currents was evident in a larger pool of WT cells used for other experiments. In conclusion, the TS2-neo mutation does not affect the functional expression of activating and noninactivating BK channels.

TS2 mutation induces cell swelling and impairs mitochondria

The drastic decrease of Nav current-density (Fig. 8), the increased membrane capacitance (Fig. 3,8) and the altered AP firing (Fig. 6,7) cannot be simply attributed to changes of Cav1.2 channel gating. Some secondary structural changes may occur in mutated MCCs, triggered by the increased Ca^{2+} entering the cell through Cav1.2-mutated channels (Fig. 5d). Conventional electron microscopy was used to view the ultrastructure of CCs in intact adrenal medulla glands of WT and TS2-neo mice (Salio *et al.*, 2017). TEM images exhibited remarkable structural changes at both the nuclear (Nu) and cytoplasmic levels (Fig. 10a). Nuclei of TS2-neo MCCs had a more heterochromatic appearance than WT MCCs. TS2-neo MCCs showed also large areas of vacuolization, conferring a more electron-lucent appearance, as well as an apparent reduction of intracellular organelles (Fig. 10a). Mitochondria (mit) were abundant and densely distributed at the perinuclear and cortical regions in WT MCCs (Villanueva *et al.*, 2014), but their density was strongly reduced in CCs of TS2-neo (0.05 ± 0.003 N/µm^2, n= 50 vs. WT-MCCs (0.22 ± 0.01 N/µm^2, n= 50; Mann-Whitney test, ****p< 0.0001). Mitochondria of mutant mice had also altered ultrastructure, exhibiting a reduced number of cristae when compared with WT MCCs (Fig. 10a). In addition, the density of large dense-core granules (LDCGs) was significantly lower in the cytoplasm of TS2-neo MCCs (1.81 ± 0.09 N/µm^2, n= 50) compared to WT-MCCs (3.00 ± 0.17 N/µm^2, n= 50; Mann-Whitney test, ****p< 0.0001). In mutant mice, LDCGs were visibly separated from their perigranular membrane by a swollen electron-lucent space.

The abundant vacuolization observed in nearly all TS2-neo mutated cells suggested a marked cell swelling, in agreement with the cell capacitance increases. We calculated the area of the cell profiles visible in single sections and found that the histograms of WT (grey bars) and TS2-neo cell areas (light-dark red bars) had different means: 113.3 μm^2 (WT; n= 50) and 140.2 μm^2 (TS2-neo; n= 50) (Mann-Whitney test, ****p< 0.0001) (Fig. 10b). Thus, TS2-neo cells undergo marked swelling that increases the cell surface area by ~24%, which is comparable to the estimated increase of membrane capacitance (~19%).

Mitochondria function was further assayed by measuring: 1) the electron flux between complex I and III of the mitochondrial respiratory chain as a measure of mitochondrial metabolic activity (Fig. 10c-left), 2) the mitochondria electrochemical potential to assay the percentage of damaged mitochondria (Fig. 10c-middle) and, 3) the levels of mitochondrial ATP produced by the electron transport chain (Fig. 10c-right) (Riganti *et al.*, 2015). All three parameters were markedly altered in the TS2-mutated MCCs. The electron flux between complex I and III and the synthesis of mitochondrial ATP were drastically reduced (***p< 0.001), while the percentage of damaged cells increased (***p< 0.001) due to a sustained mitochondrial depolarization in TS2-neo cells. Thus, mitochondrial metabolism appears significantly impaired in TS2-neo cells, justifying the severe ultrastructural changes of mutated MCCs. We also tested whether the reduced mitochondria metabolism could drive any mitochondrial-dependent apoptotic machinery. To test this, we prepared sections of adrenal glands derived from WT and TS2-neo mice for TUNEL and DAPI assays to reveal apoptotic cells (Fig. 10d). No significant differences were observed, either in the cortical or in the medulla areas. The amounts of TUNEL positive cells and/or picnotic nuclei were similar. This excludes that the altered mitochondria metabolism may induce massive cell death.

Ca^{2+}-dependent secretion is attenuated in TS2-mutated MCCs

The altered morphology of secretory granules also suggested that the Ca^{2+}-dependent secretion of catecholamines may be altered in TS2-mutated MCCs. We therefore tested how the mutation affects the depolarization-evoked capacitance increases (ΔC) and the size of the readily-releasable pool (RRP) of vesicles (Carabelli *et al.*, 2003; Marcantoni *et al.*, 2009; Gosso *et al.*, 2011). In WT-MCCs, step depolarization of 100 ms to +10 mV induced a mean ΔC of 26.5 fF (n= 12) that decreased to 13.0 fF (n= 16) in TS2-neo MCCs (**p< 0.01), suggesting a significant decrease of vesicle secretion despite the maintained average quantity of Ca^{2+} charge (Q) at

comparable levels in WT and TS2-neo cells (Fig. 11a,b). A similar ΔC reduction was observed at 0 mV where the mean ΔC decreased from 24.4 (n= 11) to 10.8 fF (n= 13) (Fig. 11a, b). These data were obtained by repeating 2 to 3 times the 100 ms depolarizations to +10 and 0 mV, separated by 60 s to allow full replenishment of the ready releasable pool between stimulations (Carabelli *et al.*, 2003; Gavello *et al.*, 2013). Mean values of ΔC for each cell were used to calculate the mean ΔC at +10 and 0 mV. By plotting each ΔC versus the Ca^{2+} charge density (pC/pF) we estimated also the Ca^{2+}-dependence of the secretory response (Fig. 11c) (see also Fig. 6b in Gavello et al., 2013). The slope of the linear Ca^{2+}-dependence of secretion was 8.0 ± 1.1 fF/(pC/pF) in WT MCCs (black line) and decreased to 3.2 ± 0.5 fF/(pC/pF) in TS2-neo mutated cells (red line; ***p< 0.001). This suggests reduced Ca^{2+}-sensitivity of secretion, most likely due to the altered intracellular Ca^{2+}-dependent pathways of mutated cells (Fig. 3e, 10a).

The size of the RRP and the probability of vesicle release (Pr) were determined using a double-pulse protocol consisting of two consecutive pulses of 100 ms of equal amounts of Ca^{2+} charges, quickly delivered to avoid vesicle replenishment (Gillis *et al.*, 1996; Carabelli *et al.*, 2003). From the ΔC measured at the end of the two pulses (ΔC_1, ΔC_2; Fig. 11d) we calculated $B_{max}= (\Delta C_1 + \Delta C_2)/(1 - (\Delta C_2/\Delta C_1)^2$ corresponding to the size of the RRP and $P_r= 1-(\Delta C_2/\Delta C_1)$. We found that TS2-neo and WT-MCCs possess similar RRPs of ~33 fF but distinct P_r (Fig. 11e). P_r was ~25% smaller in TS2-neo MCCs, suggesting that the reduced catecholamines secretion in TS2-mutated cells is likely due to a decreased rate of vesicle release associated with the decreased Ca^{2+}-dependence of secretion.

The Cav1.2 blocker verapamil rescues AP burst firing in TS2-neo MCCs

To demonstrate that the altered excitability of TS2-mutated MCCs derives from an increased Ca^{2+} entry through less inactivating Cav1.2 channels, we tested whether common L-type channel blockers could rescue the normal firing of mutated MCCs by reducing Ca^{2+} influx at rest and during cell activity. We first tested if chronically applied verapamil (5-15 µM) could help rescuing the normal firing of mutated MCCs. Verapamil is a benzothiazepine that blocks Cav1 channels with high affinity when open (Lee & Tsien, 1983). First, however, we tested whether verapamil effectively blocked AP firing when applied acutely on WT-MCCs. In n= 5 cells, we found that acute application of 5 to 15 µM verapamil hyperpolarized the cells by ~8 mV and reversibly blocked AP firing (Fig. 12).

Overnight application (18 h) of 15 µM verapamil was sufficient to rescue the normal burst firing of mutated MCCs (Fig. 13a). The rescued firing was characterized by an increased 1st peak amplitude overshoot (+17.7 mV, n= 4 vs. −15.6 mV, n= 7; verapamil-treated vs. TS2-neo MCCs; ***p< 0.001) and by an increased last peak amplitude (−14.0 mV vs. −24.9 mV; **p< 0.01) (Fig. 13b). In agreement with these observations, the mean plateau amplitude was also more positive (−24.2 mV vs. −37.9 mV; **p< 0.01) and the number of events within a burst returned to normal (4.5 vs 2.7; **p< 0.01) (Fig. 13b). Interestingly, verapamil worked at relatively high-doses (15 µM) and was unable to rescue the tonic repetitive firing observed in ~65% of WT-MCCs (Fig. 6). Lower doses of verapamil (1-5 µM) failed to rescue normal AP firing (n= 8).

The Cav1.2 blocker nifedipine rescues the normal AP firing in TS2-neo MCCs

The inability of verapamil to rescue normal tonic firing suggested that Cav1 blockers like nifedipine, which blocks Cav1.2 channels in the closed and inactivated state (Bean, 1984), might be more effective. Preliminary attempts using high-doses of nifedipine (from 15 to 1 µM) were ineffective. Presumably, due to their toxic effects on MCCs survival. We thus reduced the DHP concentration to 0.3 µM to block 40% of the L-type current in MCCs (Marcantoni *et al.*, 2010; Mahapatra *et al.*, 2011). Overnight incubation of TS2-mutated cells with 0.3 µM nifedipine (18 to 42 h) restored the normal repetitive firing. After washout of the DHP, 70% of n= 23 pretreated cells exhibited single repetitive APs with clear overshoot (Fig. 13c), 13% underwent burst firing and 17% had no activity. These percentages were similar to those observed in WT cells and significantly different from TS2-neo (Fig. 13d; *p< 0.05 and **p< 0.01; Chi square test). Concerning the tonic firing, overnight pretreatment with 0.3 µM nifedipine caused an increased peak amplitude that was comparable to WT MCCs (55.2 ± 2.8 mV, n= 16; Fig. 13e), while the half-width (4.0 ± 0.4 ms) and antipeak amplitude (−8.3 ± 1.2 mV) remarkably recovered compared with TS2-mutated cells (**p< 0.01; Fig. 13e). In conclusion, 18-42 h incubation with nifedipine was able to rescue the normal repetitive firing of mutated MCCs.

To assess whether chronic treatment with nifedipine was beneficial only on TS2-mutated cells with altered resting Ca^{2+}-influx, and not a general positive consequence of the DHP on normal MCCs, we tested the effects of chronic nifedipine (18 to 42 h) in WT MCCs. Visual inspection under the microscope revealed that most nifedipine-treated WT cells were swelled, vacuolated and had unclear membrane borders. In current-clamp recordings after DHP washout, we found that over a total of n= 14 nifedipine-treated MCCs, 8 cells did not seal, 6 cells were depolarized

(mean V_{rest}= -43.2 mV) and had no AP activity at rest. Of the latter group of cells, only two of them fired a single AP after 5-10 s hyperpolarization to -65, -70 mV and subsequent depolarization to their resting potential (Fig. 14a). As a control, in 4 out of 4 nifedipine-untreated WT MCCs we could record the normal spontaneous repetitive firing shown in Fig. 6d, with overshoot APs (*not shown*). We conclude that partial block of L-type channels for 18-42 h with 0.3 µM nifedipine completely abolishes the spontaneous repetitive firing and is therefore toxic for WT MCCs.

All the above experiments were carried out after chronic treatment with nifedipine and in the absence of the DHP during current-clamp recordings. Cell dishes were washed with Tyrode standard solution, which was the extracellular solution for these recordings. To ensure that the effects of nifedipine were due to the chronic treatment and not to an acute action of any residual nifedipine, in a series of experiments we tested the effects of acute application of the DHP on TS2-mutated cells. Acute application of 3 µM nifedipine fully blocked the activity of all the TS2-mutated cells tested (n= 5), regardless of their firing mode (tonic or bursts) (Fig. 14b_1). The blocking action was immediate (2-3 s) and persisted for the entire duration of the application (> 60 s) as previously reported on WT MCCs (Marcantoni *et al.*, 2010; Vandael *et al.*, 2010; Guarina *et al.*, 2017). Application of 0.3 µM nifedipine in other TS2-mutated cells was variable. In 3 cells out of 6 the DHP fully blocked the activity (Fig. 14b_2), while in the remaining 3 cells nifedipine caused a small depolarization of about 5 mV followed by a reduced frequency of AP firing. In conclusion, acute application of nifedipine (3 to 0.3 µM) caused a depressive action on AP firing similar to that observed in WT MCCs.

Overnight incubations with nifedipine rescues the density and steady-state inactivation of Nav channels and Ca^{2+}-dependent secretion of TS2-neo MCCs

Recovery of the AP firing after chronic incubation with nifedipine suggests that the density of functional Nav channels recovers during the DHP treatment. Fig. 15a clearly shows that the mean maximum of the *dV/dt* vs. *V* phase-plane plot calculated on the first AP (50.1 V/s; n= 16) is comparable with that of WT MCCs on the same panel (41 V/s; n= 10) and in Fig. 6g (48.5 V/s; n= 7). Although this is already highly indicative of an increased density of functional Nav channels, we also checked whether the size, time course and voltage-dependent properties of Nav currents recovered during the DHP-treatment. Fig. 15b shows that Nav current amplitudes recovered partially following the overnight incubation with nifedipine (1.1 ± 0.06 nA, n = 11,

TS2+nife vs. 0.87 ± 0.07 nA; n= 13; TS2-neo; *p< 0.05) while membrane capacitance was not significantly different from TS2-neo mutated cells. The mean density of Nav currents increased by ~ 30%: from 129.9 to 187.8 pA/pF (*p< 0.05). Activation and inactivation time course was not altered (Fig. 15c) and the same occurred to the voltage-dependence of I/V relationships (blue triangles in Fig. 15d) that was similar to that of WT (dashed black curve) and TS2-neo mutated cells (red circles). The voltage dependence of fast inactivation was unchanged (not shown) while the voltage-dependence of steady-states inactivation recovered partially (blue triangles vs red circles in Fig. 15e), to become nearly indistinguishable from the SSI of WT cells (dashed black curve). The red and blue curves had nearly the same $V_{1/2}$ (- 28 mV TS2+nife vs. -30 mV TS2-neo cells) but well separated minimum values (0.52 TS2+nife and 0.43 TS2-neo cells at +30 mV). In conclusion, it appears that the recovery of AP firing after overnight nifedipine application was paralleled by a robust recovery of functional Nav channels.

Chronic treatment with nifedipine recovers also the secretory activity of MCCs measured through membrane capacitance changes (ΔC). In Fig. 15f are shown typical recordings of ΔC following 100 ms step depolarization to +10 and 0 mV, highlighting how overnight incubation with 0.3 µM nifedipine rescues the secretory activity of TS2-neo mutated cells. After chronic treatment and washout of the DHP, on average ΔC increased from 13.0 (n= 16) to 28.9 fF (n= 9; **p< 0.01) at + 10 mV and from 10.8 fF (n=13) to 20.2 mV at 0mV (n= 9; **p< 0.01) (Fig. 15g) while the quantity of Ca^{2+} charges (Q) remained nearly unchanged and comparable to those in WT cells. As for WT and TS2-neo mutated cells, we plotted ΔC versus the Ca^{2+} charge density to estimated the Ca^{2+}-dependence of the secretory response (Fig. 15h). The slope of the linear Ca^{2+}-dependence of secretion was 3.2 ± 0.5 fF/(pC/pF) in TS2-neo MCCs (red line) and increased to 7.7 ± 0.7 fF/(pC/pF) in nifedipine-treated TS2-neo cells (blue line; ***p< 0.001). Thus, the Ca^{2+}-sensitivity of secretion in TS2-mutated cells is driven by altered L-type channel-dependent mechanisms that are recovered by chronic nifedipine application.

Discussion

We provided evidence that the TS2-neo mouse (Bader *et al.*, 2011) is a suitable murine model for studying the molecular bases of altered MCC function associated with the G406R point mutation of *CACNA1C* gene. The mutation reduces L-type channel inactivation, shifts leftward the voltage-dependence of channel activation and inactivation, thus increasing the resting

window Ca^{2+} current. These gating changes reduce the mitochondrial function, alter cell firing and decrease catecholamine secretion. Chronic application of L-type channel blockers is sufficient to rescue Na_V channel density, normal spontaneous firing and Ca^{2+}-dependent secretion of chromaffin cells, thus anticipating possible therapeutic treatments for the forms of ASD associated with TS.

The decrease of L-type channel inactivation is surprisingly small in mutated MCCs: 10-25% of the total Ca^{2+} current after 1 s. This is in good agreement with what expected, considering that Cav1.2 contributes to about half of the total L-type Ca^{2+} current (Marcantoni *et al.*, 2010; Vandael *et al.*, 2010) and that exon 8 contributes to 20% of the Cav1.2 channel expression in WT and 50% in heterozygous mutated mice. In heterozygous mice, the expression ratio of mutated vs WT channels varies between 1:1 and 1:5 (Fig. 2), and thus we expected inactivation changes varying between 10 and 25%. Our data are in relatively good agreement with previous findings showing that in heterologous systems, full expression of the G406R Cav1.2 mutation causes nearly complete loss of VDI (Fig. 5G,H in Splawski et al (2004)). Expression of 50% G406R and 50% WT Cav1.2 channels, as it occurs in heterozygous mice, would predict only a 50% loss of VDI and a further 50% reduction, due an equal contribution of Cav1.3 and Cav1.2 channels to total current, decreases further the change to 25%. Given the great variability and functional differences between heterologously expressed and native Cav1.2 channels, the reported small change on VDI observed in TS2-mutated MCCs appears consistent. Concerning the ~-5 mV leftward shift of L-type current activation in TS2 mutated MCCs, the shift appears significantly smaller and in line with the ~-10 mV shift reported for the human G406R-mutated Cav1.2 channel fully expressed in HEK293 cells (Dick *et al.*, 2016) and the ~-14 mV shift for the rabbit G436R-mutated Cav1.2 channel fully expressed in *Xenopus laevis* oocytes (Raybaud *et al.*, 2006).

Given this, our goal was to find the mechanism of how small changes of L-type channel inactivation impair MCC firing and secretion. Our conclusion is that L-type channels contribute to ~50% of the total Ca^{2+} current and play a critical role in the regulation of MCC firing. Cav1.3 and Cav1.2 regulate the inward pacemaking current that generates spontaneous (Marcantoni *et al.*, 2010; Vandael *et al.*, 2010) or evoked repetitive firing (Vandael *et al.*, 2012). Thus, a small continuous increase (over days) of the resting pacemaking current induced by the mistuned Cav1.2 channel inactivation is sufficient to trigger a number of Ca^{2+}-dependent pathways that affect cell function (Voronina *et al.*, 2015). This includes a decreased density of Na_V channels and

an increase of their SSI that resembles the protein kinase-dependent reduction of $Na_V1.2$ channels availability induced by neurotransmitters (Carr *et al.*, 2003).

Treatment with nifedipine recovers the altered firing of TS2-mutated MCCs by rescuing Na_V channel density and steady-state inactivation

We have shown that the TS2 mutation drastically alters the firing properties of MCCs. Most TS2-mutated cells fire in bursts while a minority undergo repetitive firing below overshoot (Fig. 6,7). This is markedly different from the firing modes of most WT cells that exhibit normal tonic firing and a small fraction that undergoes burst firing (Vandael *et al.*, 2015b). Burst firing in WT-MCCs occurs during altered physiological conditions (Martinez-Espinosa *et al.*, 2014; Vandael *et al.*, 2015a; Vandael *et al.*, 2015b; Guarina *et al.*, 2017) (for a review see (Lingle *et al.*, 2018)). Specifically, when: 1) Na_V channels are steadily inactivated, 2) K^+ permeable channels (BK, TASK1-3) are blocked, 3) inward L-type currents are increased or 4) following deletion of BK-β_2 subunit that completely abolishes BK channel inactivation. Some of these conditions occur in TS2-mutated cells. The density of Na_V1 channel is largely reduced and SSI is increased. Consequently, APs are smaller and broader decreasing the activation of BK and K_V channels. This favors a less complete repolarization and the formation of a plateau phase that sustain AP bursts. TS2-mutated Cav1.2 channels contribute further to stabilize burst firing. They inactivate less completely and stay more open during the plateau phase because of the increased "window" current. This contributes significantly to sustain AP bursts of 300-400 ms duration because of the Cav1.2 reduced inactivation. A possible cause for the increased burst firing in TS2-mutated MCCs could derive also from the strong attenuation of BK channel inactivation observed in 6 out of 10 mutated cells (Fig. 9). Removal of BK channel inactivation by deletion of the BK-β_2 subunit shifts also BK channel activation toward more positive voltages (Martinez-Espinosa *et al.*, 2014). This attenuates the activation of K_V channels that in turn slows the rising phase, lowers the amplitude and reduces the repolarization phase of APs. All this facilitates burst firing in MCCs. In conclusion, removal of BK channel inactivation could also account for the increased percentage of burst firing in TS2-neo cells. However, the ratio of TS2-mutated cells exhibiting noninactivating vs inactivating channels (6:4) does not appear significantly different from WT cells (4:4), making this possibility less likely for TS2-neo MCCs.

A key observation from our work is that overnight incubations of TS2-mutated cells with either verapamil or nifedipine, are able to rescue the normal firing of WT-MCCs. Nifedipine at 300 nM

concentration rescued the normal tonic firing of MCCs (Fig. 13c). At lower doses (<100 nM) the DHP application was ineffective while at higher doses (>3 µM) it was toxic for cell survival. Most likely due to sustained cell depolarizations induced by either the full block of L-type channels that may drastically reduce the SK currents contributing to resting potential (Vandael *et al.*, 2012) or the direct unspecific block of other K^+ channels by the DHP (Liu *et al.*, 2007). The binding of low doses of nifedipine to the inactivated state of L-type channels (Bean, 1984; Sanguinetti & Kass, 1984; Uehara & Hume, 1985) is favored by the spontaneous burst firing of mutated MCCs, during which Cav1.2-mutated channels are maintained at less negative potentials for longer periods. Partial block of L-type channels by chronic exposure to nifedipine is expected to attenuate for several hours the abnormal "window" current of TS2-mutated cells and to reestablish more physiological conditions that favor Na_v channel trafficking (Di Biase *et al.*, 2011), recovery of SSI and return to normal AP firing. These rescuing effects of the brain permeable blocker nifedipine on the AP firing of TS2-mutated cells are of great potential significance. They provide a rationale for experimental therapeutic attempts using clinically available Ca^{2+} channel blockers in autistic individuals harboring Cav1.2 or Cav1.3 channel mutations.

The attenuated Ca^{2+}-dependent secretion in TS2-mutated MCCs is rescued by overnight exposure to nifedipine

Catecholamine secretion in MCCs is strictly Ca^{2+}-dependent and regulated by voltage-gated Ca^{2+} channels (Garcia *et al.*, 2006; Mahapatra *et al.*, 2012). All Cav channel types expressed in CCs (L, N, P/Q, R, T) contribute to vesicle fusion and secretion proportionally to their expression density (Marcantoni *et al.*, 2008; Mahapatra *et al.*, 2012). Thus, in MCCs L-type channels contribute to half of the Ca^{2+} current and are responsible for half of the secreted catecholamines (Carabelli *et al.*, 2003; Marcantoni *et al.*, 2009). The TS2 mutation decreases markedly the amount of Ca^{2+}-induced secretion (ΔC), suggesting a reduced number of secretory granules that release their content in mutated MCCs. The reduction is associated with a decreased Ca^{2+}-dependence and a lower rate of catecholamine release (*Pr)* rather than to a reduction of the RRP. A rational for this, is that part of the reduced ΔC is due to the swelling induced by the TS2-mutation that reduces the Ca^{2+}-dependence and *Pr* by reducing the density of Ca^{2+} channels around the secretory sites. Part of the ΔC reduction could be also associated with some TS2-modified structural element of the complex secretory apparatus that regulates the priming, docking and

fusion of LDCGs (Jahn & Sudhof, 1999; Dhara *et al.*, 2018). An interesting finding of our study is that overnight treatment with nifedipine helps rescuing both the amount of Ca^{2+}-dependent secretion and its physiological Ca^{2+}-dependence, confirming once more that the dysfunction of TS2-mutated MCCs originates from the resting influx of Ca^{2+} through Cav1.2 mutated channels. Future works will clarify how this occurs at the molecular level.

The altered neurotransmitter release induced by TS2-mutated Cav1.2 channels suggests the intriguing possibility that similar changes could occur on brain synapses. Cav1.2 and Cav1.3 do not contribute to the synchronous neurotransmitter release in central synapses (Simms & Zamponi, 2014; Zamponi, 2016) but regulate the Ca^{2+} required for vesicle replenishment (Okita *et al.*, 2000; Fourcaudot *et al.*, 2009; Zorrilla de San Martin *et al.*, 2010; Zhang *et al.*, 2015). Compelling evidence suggests that synaptic neurotransmission shares common molecular elements with the secretory apparatus of CCs (Jahn & Fasshauer, 2012; Neher, 2018). Thus, pre-synaptic mistuning at brain synapses could be a further cause of ASD associated with Cav1.2 mutations.

Cav1.2 G406R and Cav1.3 missense mutations associated with ASD share similar gating mechanisms and cell signalings

We have shown that TS2-mutated MCCs exhibit reduced inactivation and leftward shifts of L-type channel activation and inactivation. Similar effects are shown for the V401L Cav1.3 mutation associated with ASD (Pinggera *et al.*, 2017), suggesting common pathogenic mechanisms of Cav1.2 and Cav1.3 mutations. Mutations G406R and V401L occur at the IS6 helix, reduce channel inactivation and shift leftward the voltage-dependence of activation and inactivation. A second Cav1.3 mutation (A749G) also causes autism (Pinggera *et al.*, 2015) but has only partial analogy with G406R. It occurs on the IIS6 helix, exhibits similar leftward shifts of activation and inactivation, but in contrast to G406R it enhances Cav1.3 channel inactivation. It is therefore likely that it is not the rate of channel inactivation but the "leftward" shifts of activation and inactivation that is the triggering cause of ASD. This conclusion is also supported by the observation that, despite the G406R and G402S mutations reduce Cav1.2 channel inactivation, only G406R produces ASD (Splawski *et al.*, 2005). Indeed, the G402S mutation causes a "positive" shift of activation and G402S patients are neurologically intact (Frohler *et al.*, 2014; Tallila *et al.*, 2014; Hiippala *et al.*, 2015).

How the negative voltage shift of Cav1 channel activation may alter the excitation/inhibition balance, synaptic plasticity and neuronal development remains to be clarified. One possibility is that Cav1 gain-of-function mutations directly alter synapse and dendritic spine stability (Stanika *et al.*, 2016). Alternatively, autistic symptoms may derive from a mistuning of the Cav1.2-mediated transcription signals associated with Ca^{2+}-signals followed by voltage-dependent conformational changes (VΔC) of Cav1.2 channel opening (Li *et al.*, 2016). In this view, it is of key importance to understand how the leftward shift of activation alters AP firing in central neurons during neurogenesis, when Cav1.2 and Cav1.3 channel expression progressively changes with time (Fabel & Kempermann, 2008; Marschallinger *et al.*, 2015). The negatively shifted activation may likely affect the percentage of excitable neurons, the shape and frequency of APs and the type of firing (tonic vs. burst, as in MCCs), with consequent altered synaptogenesis and excitation/inhibition balance of neuronal microcircuits (Ben-Ari & Spitzer, 2010). If this would be the case, a search for a new class of Ca^{2+} channel modulators that shift "rightward" the activation of Cav1.2 L-type channels would be even more beneficial as therapeutics for ASD than most common DHP antagonists that block unspecifically all Cav1 channels. Further studies will clarify these issues.

References

Bader PL, Faizi M, Kim LH, Owen SF, Tadross MR, Alfa RW, Bett GC, Tsien RW, Rasmusson RL & Shamloo M. (2011). Mouse model of Timothy syndrome recapitulates triad of autistic traits. *Proceedings of the National Academy of Sciences of the United States of America* **108,** 15432-15437.

Baldelli P, Hernandez-Guijo JM, Carabelli V, Novara M, Cesetti T, Andres-Mateos E, Montiel C & Carbone E. (2004). Direct and remote modulation of L-channels in chromaffin cells - Distinct actions on alpha(1C) and alpha(1D) subunits? *Molecular Neurobiology* **29,** 73-96.

Barnabei VM, Rasmusson RL & Bett GC. (2014). Autism and induced labor: is calcium a potential mechanistic link? *American journal of obstetrics and gynecology* **210,** 494-495.

Barrett CF & Tsien RW. (2008). The Timothy syndrome mutation differentially affects voltage- and calcium-dependent inactivation of CaV1.2 L-type calcium channels. *Proceedings of the National Academy of Sciences of the United States of America* **105,** 2157-2162.

Bean BP. (1984). Nitrendipine block of cardiac calcium channels: high-affinity binding to the inactivated state. *Proceedings of the National Academy of Sciences of the United States of America* **81,** 6388-6392.

Ben-Ari Y & Spitzer NC. (2010). Phenotypic checkpoints regulate neuronal development. *Trends in neurosciences* **33,** 485-492.

Bett GC, Lis A, Wersinger SR, Baizer JS, Duffey ME & Rasmusson RL. (2012). A Mouse Model of Timothy Syndrome: a Complex Autistic Disorder Resulting from a Point Mutation in Cav1.2. *North American journal of medicine & science* **5,** 135-140.

Bianchi FT, Tocco C, Pallavicini G, Liu Y, Verni F, Merigliano C, Bonaccorsi S, El-Assawy N, Priano L, Gai M, Berto GE, Chiotto AM, Sgro F, Caramello A, Tasca L, Ala U, Neri F, Oliviero S, Mauro A, Geley S, Gatti M & Di Cunto F. (2017). Citron Kinase Deficiency Leads to Chromosomal Instability and TP53-Sensitive Microcephaly. *Cell reports* **18,** 1674-1686.

Bidaud I & Lory P. (2011). Hallmarks of the channelopathies associated with L-type calcium channels: a focus on the Timothy mutations in Ca(v)1.2 channels. *Biochimie* **93,** 2080-2086.

Campia I, Lussiana C, Pescarmona G, Ghigo D, Bosia A & Riganti C. (2009). Geranylgeraniol prevents the cytotoxic effects of mevastatin in THP-1 cells, without decreasing the beneficial effects on cholesterol synthesis. *British journal of pharmacology* **158,** 1777-1786.

Carabelli V, Giancippoli A, Baldelli P, Carbone E & Artalejo AR. (2003). Distinct potentiation of L-type currents and secretion by cAMP in rat chromaffin cells. *Biophysical journal* **85,** 1326-1337.

Carabelli V, Marcantoni A, Comunanza V, De Luca A, Diaz J, Borges R & Carbone E. (2007). Chronic hypoxia up-regulates alpha(1H) T-type channels and low-threshold catecholamine secretion in rat chromaffin cells. *The Journal of physiology* **584,** 149-165.

Carr DB, Day M, Cantrell AR, Held J, Scheuer T, Catterall WA & Surmeier DJ. (2003). Transmitter modulation of slow, activity-dependent alterations in sodium channel availability endows neurons with a novel form of cellular plasticity. *Neuron* **39,** 793-806.

Cesetti T, Hernandez-Guijo JM, Baldelli P, Carabelli V & Carbone E. (2003). Opposite action of beta 1- and beta 2-adrenergic receptors on Ca(V)1 L-channel current in rat adrenal chromaffin cells. *The Journal of Neuroscience* **23,** 73-83.

Dhara M, Mohrmann R & Bruns D. (2018). v-SNARE function in chromaffin cells. *Pflugers Archiv : European journal of physiology* **470,** 169-180.

Di Biase V, Tuluc P, Campiglio M, Obermair GJ, Heine M & Flucher BE. (2011). Surface traffic of dendritic CaV1.2 calcium channels in hippocampal neurons. *The Journal of neuroscience : the official journal of the Society for Neuroscience* **31,** 13682-13694.

Dick IE, Joshi-Mukherjee R, Yang W & Yue DT. (2016). Arrhythmogenesis in Timothy Syndrome is associated with defects in Ca(2+)-dependent inactivation. *Nat Commun* **7,** 10370.

Ehlinger DG & Commons KG. (2017). Altered Cav1.2 function in the Timothy syndrome mouse model produces ascending serotonergic abnormalities. *The European journal of neuroscience* **46,** 2416-2425.

Erxleben C, Liao Y, Gentile S, Chin D, Gomez-Alegria C, Mori Y, Birnbaumer L & Armstrong DL. (2006). Cyclosporin and Timothy syndrome increase mode 2 gating of CaV1.2 calcium channels through aberrant phosphorylation of S6 helices. *Proceedings of the National Academy of Sciences of the United States of America* **103,** 3932-3937.

Fabel K & Kempermann G. (2008). Physical Activity and the Regulation of Neurogenesis in the Adult and Aging Brain. *Neuromol Med* **10,** 59-66.

Fourcaudot E, Gambino F, Casassus G, Poulain B, Humeau Y & Luthi A. (2009). L-type voltage-dependent Ca(2+) channels mediate expression of presynaptic LTP in amygdala. *Nat Neurosci* **12,** 1093-1095.

Frohler S, Kieslich M, Langnick C, Feldkamp M, Opgen-Rhein B, Berger F, Will JC & Chen W. (2014). Exome sequencing helped the fine diagnosis of two siblings afflicted with atypical Timothy syndrome (TS2). *BMC medical genetics* **15,** 48.

Garcia AG, Garcia-De-Diego AM, Gandia L, Borges R & Garcia-Sancho J. (2006). Calcium signaling and exocytosis in adrenal chromaffin cells. *Physiol Rev* **86,** 1093-1131.

Gavello D, Fenoglio I, Fubini B, Cesano F, Premoselli F, Renna A, Carbone E & Carabelli V. (2013). Inhibition of catecholamine secretion by iron-rich and iron-deprived multiwalled carbon nanotubes in chromaffin cells. *Neurotoxicology* **39,** 84-94.

Gavello D, Vandael D, Gosso S, Carbone E & Carabelli V. (2015). Dual action of leptin on rest-firing and stimulated catecholamine release via phosphoinositide 3-kinase-driven BK channel up-regulation in mouse chromaffin cells. *The Journal of physiology* **593,** 4835-4853.

Gillis KD, Mossner R & Neher E. (1996). Protein kinase C enhances exocytosis from chromaffin cells by increasing the size of the readily releasable pool of secretory granules. *Neuron* **16,** 1209-1220.

Gosso S, Gavello D, Giachello CNG, Franchino C, Carbone E & Carabelli V. (2011). The effect of CdSe-ZnS quantum dots on calcium currents and catecholamine secretion in mouse chromaffin cells. *Biomaterials* **32,** 9040-9050.

Guarina L, Vandael DH, Carabelli V & Carbone E. (2017). Low pHo boosts burst firing and catecholamine release by blocking TASK-1 and BK channels while preserving Cav1 channels in mouse chromaffin cells. *The Journal of physiology* **595,** 2587-2609.

Hiippala A, Tallila J, Myllykangas S, Koskenvuo JW & Alastalo TP. (2015). Expanding the phenotype of Timothy syndrome type 2: an adolescent with ventricular fibrillation but normal development. *American journal of medical genetics Part A* **167a,** 629-634.

Jahn R & Fasshauer D. (2012). Molecular machines governing exocytosis of synaptic vesicles. *Nature* **490,** 201-207.

Jahn R & Sudhof TC. (1999). Membrane fusion and exocytosis. *Annual review of biochemistry* **68,** 863-911.

Jo S & Bean BP. (2017). Lacosamide Inhibition of Nav1.7 Voltage-Gated Sodium Channels: Slow Binding to Fast-Inactivated States. *Molecular pharmacology* **91,** 277-286.

Kawaida M, Abe T, Nakanishi T, Miyahara Y, Yamagishi H, Sakamoto M & Yamada T. (2016). A case of Timothy syndrome with adrenal medullary dystrophy. *Pathology international* **66,** 587-592.

Krey JF, Pasca SP, Shcheglovitov A, Yazawa M, Schwemberger R, Rasmusson R & Dolmetsch RE. (2013). Timothy syndrome is associated with activity-dependent dendritic retraction in rodent and human neurons. *Nat Neurosci* **16,** 201-209.

Lee KS & Tsien RW. (1983). Mechanism of calcium channel blockade by verapamil, D600, diltiazem and nitrendipine in single dialysed heart cells. *Nature* **302,** 790-794.

Li B, Tadross MR & Tsien RW. (2016). Sequential ionic and conformational signaling by calcium channels drives neuronal gene expression. *Science (New York, NY)* **351,** 863-867.

Lingle CJ, Martinez-Espinosa PL, Guarina L & Carbone E. (2018). Roles of Na(+), Ca(2+), and K(+) channels in the generation of repetitive firing and rhythmic bursting in adrenal chromaffin cells. *Pflugers Archiv : European journal of physiology* **470,** 39-52.

Liu H, Enyeart JA & Enyeart JJ. (2007). Potent inhibition of native TREK-1 K+ channels by selected dihydropyridine Ca2+ channel antagonists. *The Journal of pharmacology and experimental therapeutics* **323,** 39-48.

Mahapatra S, Calorio C, Vandael DHF, Marcantoni A, Carabelli V & Carbone E. (2012). Calcium channel types contributing to chromaffin cell excitability, exocytosis and endocytosis. *Cell Calcium* **51,** 321-330.

Mahapatra S, Marcantoni A, Vandael DHF, Striessnig J & Carbone E. (2011). Are Ca(v)1.3 pacemaker channels in chromaffin cells? Possible bias from resting cell conditions and DHP blockers usage. *Channels* **5,** 219-224.

Marcantoni A, Baldelli P, Hernandez-Guijo JM, Comunanza V, Carabelli V & Carbone E. (2007). L-type calcium channels in adrenal chromaffin cells: Role in pace-making and secretion. *Cell Calcium* **42,** 397-408.

Marcantoni A, Carabelli V, Comunanza V, Hoddah H & Carbone E. (2008). Calcium channels in chromaffin cells: focus on L and T types. *Acta Physiologica* **192,** 233-246.

Marcantoni A, Carabelli V, Vandael DH, Comunanza V & Carbone E. (2009). PDE type-4 inhibition increases L-type Ca2+ currents, action potential firing, and quantal size of exocytosis in mouse chromaffin cells. *Pflugers Archiv-European Journal of Physiology* **457,** 1093-1110.

Marcantoni A, Vandael DHF, Mahapatra S, Carabelli V, Sinnegger-Brauns MJ, Striessnig J & Carbone E. (2010). Loss of Cav1.3 Channels Reveals the Critical Role of L-Type and BK Channel Coupling in Pacemaking Mouse Adrenal Chromaffin Cells. *The Journal of Neuroscience* **30,** 491-504.

Marschallinger J, Sah A, Schmuckermair C, Unger M, Rotheneichner P, Kharitonova M, Waclawiczek A, Gerner P, Jaksch-Bogensperger H, Berger S, Striessnig J, Singewald N, Couillard-Despres S & Aigner L. (2015). The L-type calcium channel Cav1.3 is required for proper hippocampal neurogenesis and cognitive functions. *Cell Calcium* **58,** 606-616.

Martinez-Espinosa PL, Yang C, Gonzalez-Perez V, Xia XM & Lingle CJ. (2014). Knockout of the BK beta2 subunit abolishes inactivation of BK currents in mouse adrenal chromaffin cells and results in slow-wave burst activity. *The Journal of general physiology* **144,** 275-295.

Neher E. (2018). Neurosecretion: what can we learn from chromaffin cells. *Pflugers Archiv : European journal of physiology* **470,** 7-11.

Okita M, Watanabe Y, Taya K, Utsumi H & Hayashi T. (2000). Presynaptic L-type Ca(2)+ channels on excessive dopamine release from rat caudate putamen. *Physiology & behavior* **68,** 641-649.

Pasca SP, Portmann T, Voineagu I, Yazawa M, Shcheglovitov A, Pasca AM, Cord B, Palmer TD, Chikahisa S, Nishino S, Bernstein JA, Hallmayer J, Geschwind DH & Dolmetsch RE. (2011). Using iPSC-derived neurons to uncover cellular phenotypes associated with Timothy syndrome. *Nat Med* **17,** 1657-U1176.

Pinggera A, Lieb A, Benedetti B, Lampert M, Monteleone S, Liedl KR, Tuluc P & Striessnig J. (2015). CACNA1D de novo mutations in autism spectrum disorders activate Cav1.3 L-type calcium channels. *Biol Psychiatry* **77,** 816-822.

Pinggera A, Mackenroth L, Rump A, Schallner J, Beleggia F, Wollnik B & Striessnig J. (2017). New gain-of-function mutation shows CACNA1D as recurrently mutated gene in autism spectrum disorders and epilepsy. *Hum Mol Genet* **26,** 2923-2932.

Raybaud A, Dodier Y, Bissonnette P, Simoes M, Bichet DG, Sauve R & Parent L. (2006). The role of the GX9GX3G motif in the gating of high voltage-activated Ca2+ channels. *The Journal of biological chemistry* **281,** 39424-39436.

Riganti C, Gazzano E, Gulino GR, Volante M, Ghigo D & Kopecka J. (2015). Two repeated low doses of doxorubicin are more effective than a single high dose against tumors overexpressing P-glycoprotein. *Cancer letters* **360,** 219-226.

Salio C, Merighi A & Bardoni R. (2017). GABAB receptors-mediated tonic inhibition of glutamate release from Abeta fibers in rat laminae III/IV of the spinal cord dorsal horn. *Molecular pain* **13,** 1744806917710041.

Sanguinetti MC & Kass RS. (1984). Voltage-dependent block of calcium channel current in the calf cardiac Purkinje fiber by dihydropyridine calcium channel antagonists. *Circulation research* **55,** 336-348.

Scharinger A, Eckrich S, Vandael DH, Schonig K, Koschak A, Hecker D, Kaur G, Lee A, Sah A, Bartsch D, Benedetti B, Lieb A, Schick B, Singewald N, Sinnegger-Brauns MJ, Carbone E, Engel J & Steiessnig J. (2015). Cell-type-specific tuning of Cav1.3 Ca2+-channels by a C-terminal automodulatory domain. *Frontiers in Cellular Neuroscience* **9,** 18.

Schlick B, Flucher BE & Obermair GJ. (2010). Voltage-activated calcium channel expression profiles in mouse brain and cultured hippocampal neurons. *Neuroscience* **167,** 786-798.

Sgro F, Bianchi FT, Falcone M, Pallavicini G, Gai M, Chiotto AM, Berto GE, Turco E, Chang YJ, Huttner WB & Di Cunto F. (2016). Tissue-specific control of midbody microtubule stability by Citron kinase through modulation of TUBB3 phosphorylation. *Cell death and differentiation* **23,** 801-813.

Simms BA & Zamponi GW. (2014). Neuronal Voltage-Gated Calcium Channels: Structure, Function, and Dysfunction. *Neuron* **82,** 24-45.

Solaro CR, Prakriya M, Ding JP & Lingle CJ. (1995). Inactivating and noninactivating Ca^{2+}- and voltage-dependent K^{+} current in rat adrenal chromaffin cells. *Journal of Neuroscience* **15,** 6110-6123.

Splawski I, Timothy KW, Decher N, Kumar P, Sachse FB, Beggs AH, Sanguinetti MC & Keating MT. (2005). Severe arrhythmia disorder caused by cardiac L-type calcium channel mutations. *Proceedings of the National Academy of Sciences of the United States of America* **102,** 8089-8096.

Splawski I, Timothy KW, Sharpe LM, Decher N, Kumar P, Bloise R, Napolitano C, Schwartz PJ, Joseph RM, Condouris K, Tager-Flusberg H, Priori SG, Sanguinetti MC & Keating MT. (2004). Ca(v)1.2 calcium channel dysfunction causes a multisystem disorder including arrhythmia and autism. *Cell* **119,** 19-31.

Stanika R, Campiglio M, Pinggera A, Lee A, Striessnig J, Flucher BE & Obermair GJ. (2016). Splice variants of the CaV1.3 L-type calcium channel regulate dendritic spine morphology. *Scientific reports* **6,** 34528.

Tallila J, Hiippala A, Myllykangas S, Alastalo T & Koskenvuo J. (2014). Timothy syndrome type 2 associated CACNA1C G402S mutation in a teenage girl with idiopathic ventricular fibrillation. *Heart, Lung and Circulation* **23, Supplement 2,** e4-e5.

Uehara A & Hume JR. (1985). Interactions of organic calcium channel antagonists with calcium channels in single frog atrial cells. *The Journal of general physiology* **85,** 621-647.

Vandael DH, Marcantoni A & Carbone E. (2015a). Cav1.3 Channels as Key Regulators of Neuron-Like Firings and Catecholamine Release in Chromaffin Cells. *Curr Mol Pharmacol* **8,** 149-161.

Vandael DH, Marcantoni A, Mahapatra S, Caro A, Ruth P, Zuccotti A, Knipper M & Carbone E. (2010). Ca(v)1.3 and BK Channels for Timing and Regulating Cell Firing. *Molecular Neurobiology* **42,** 185-198.

Vandael DH, Ottaviani MM, Legros C, Lefort C, Guerineau NC, Allio A, Carabelli V & Carbone E. (2015b). Reduced avaiy of voltage-gated sodium channels by depolarization or blockade by tetrodotoxin boosts burst firing and catecholamine release in mouse chromaffin cellslabilit. *The Journal of physiology* **593,** 905-927.

Vandael DHF, Zuccotti A, Striessnig J & Carbone E. (2012). Ca(V)1.3-Driven SK Channel Activation Regulates Pacemaking and Spike Frequency Adaptation in Mouse Chromaffin Cells. *Journal of Neuroscience* **32,** 16345-16359.

Vandesompele J, De Preter K, Pattyn F, Poppe B, Van Roy N, De Paepe A & Speleman F. (2002). Accurate normalization of real-time quantitative RT-PCR data by geometric averaging of multiple internal control genes. *Genome biology* **3,** Research0034.

Villanueva J, Viniegra S, Gimenez-Molina Y, Garcia-Martinez V, Exposito-Romero G, del Mar Frances M, Garcia-Sancho J & Gutierrez LM. (2014). The position of mitochondria and ER in relation to that of the secretory sites in chromaffin cells. *J Cell Sci* **127,** 5105-5114.

Voronina S, Collier D, Chvanov M, Middlehurst B, Beckett AJ, Prior IA, Criddle DN, Begg M, Mikoshiba K, Sutton R & Tepikin AV. (2015). The role of Ca2+ influx in endocytic vacuole formation in pancreatic acinar cells. *The Biochemical journal* **465,** 405-412.

Yarotskyy V, Gao G, Peterson BZ & Elmslie KS. (2008). The Timothy syndrome mutation of cardiac CaV1.2 (L-type) channels: multiple altered gating mechanisms and pharmacological restoration of inactivation. *The Journal of physiology* **587,** 551-565.

Zamponi GW. (2016). Targeting voltage-gated calcium channels in neurological and psychiatric diseases. *Nature reviews Drug discovery* **15,** 19-34.

Zhang H, Dong H & Lei S. (2015). Neurotensinergic augmentation of glutamate release at the perforant path-granule cell synapse in rat dentate gyrus: Roles of L-Type Ca(2)(+) channels, calmodulin and myosin light-chain kinase. *Neuropharmacology* **95,** 252-260.

Zhou Y & Lingle CJ. (2014). Paxilline inhibits BK channels by an almost exclusively closed-channel block mechanism. *Journal of General Physiology* **144,** 415-440.

Zorrilla de San Martin J, Pyott S, Ballestero J & Katz E. (2010). Ca(2+) and Ca(2+)-activated K(+) channels that support and modulate transmitter release at the olivocochlear efferent-inner hair cell synapse. *The Journal of neuroscience : the official journal of the Society for Neuroscience* **30,** 12157-12167.

Competing interests: All authors declare no competing interests.

Author contributions: CC, DG and LG performed and analyzed electrophysiological experiments. CS and MS performed electron microscopy. CR designed and performed mitochondrial metabolism assays. NTH, PT and GH designed the primers and performed RNA isolation, cDNA synthesis and qRT-PCR. FTB performed the TUNEL and DAPI assays. PD, FB and ET designed the primers and performed mouse genotyping. RLR and GCB conceived and generated the TS2-neo mouse. EC designed the study, analyzed electrophysiological experiments and wrote the manuscript with input from all co-authors. All authors have approved the final version of the manuscript.

Funding: This work was supported by Telethon Foundation (grant # GGP15110) to E.C., Austrian Science Fund (grant # SFB F4415) to G.O., A.I.R.C. (grant # IG-20107) to P.D. and (grant # IG15232) to C.R. and M.I.U.R. project "Departments of Excellence 2018 – 2022" to M.S.

Acknowledgements: We thank Dr. C. Franchino for expert technical assistance and Dr. A. Marcantoni and V. Carabelli for stimulating discussions.

Table 1 - ***Custom TaqMan gene expression assay for Cav1.2 exons 8 and 8a splice variants***

Subunit variant	GenBank number	Assay ID	Exon boundary	Sequences for custom assay
Cav1.2 ex8	NM_001255999.2	APU63XM	7-8	Fwd: 5´-GGCTGGACAGACGTGCTGTA-3´ Rev: 5´-CACCCAGGGCAACTCATAGC-3´ Probe: 5´-TGGATGCAAGACGCTAT-3´
Cav1.2 ex8a	NM_001256000.2	APWCXHJ	7-8	Fwd: 5´GGCTGGACAGACGTGCTGTA-3´ Rev: 5´- CAGGGCCAGTCCCTTCCT -3´ Probe: 5´-TGGGTCAATGATGCCG-3´

Table 2 - ***cDNA specific primer sequences for standard template cloning***

Primer name	Primer sequence
1.2 ex8/8a std fwd_SalI	5´-ATATGTCGACAGTGTCAGAACGGGACCGTG-3´
1.2 ex8/8a std rev_BglII	5´-CTTTGAGATCTTCTTCTAGTTGCTGC-3´
1.2 ex8 fusion fwd	5´-GTCAGTCTGGTCATCTTTGGATCCT-3´
1.2 ex8 fusion rev	5´-AGGATCCAAAGATGACCAGACTGAC-3´
1.2 ex8a fusion fwd	5´-GTAACACTAATCATCATAGGGTCAT-3´
1.2 ex8a fusion rev	5´-ATGACCCTATGATGATTAGTGTTAC-3´

Legends

Figure 1 – *Binding specificity of Cav1.2 exon 8 and exon 8a assays (a)* . Exon 8 and exon 8a were recognized with a high specificity (low CT value) by the corresponding assay even in the presence of a 10-fold higher concentration of the mismatching DNA fragments from exon 8a and 8, respectively. Furthermore, both assays did not recognize the similar exons 8a and 8b from Cav1.3 L-type channels. High binding specificity was confirmed by inefficient detection (high CT value) of all non-matching DNA fragments. ***Average expression stability of endogenous control genes in MCCs (b)***. All reference genes maintained comparable cDNA concentrations throughout the experiments. Data was normalized to the most stable endogenous control genes listed at the top (Gapdh and b-act).

Figure 2. *Cav1.2 exon 8 and exon 8a expression in mouse adrenal medulla.* **a.** Topology of Cav1.2 α_1-subunit showing the domain encoded by the alternative exon 8 or 8a (blue) and the position of G406R mutation on the intracellular side of IS6 segment. **b.** Amino acid sequence alignment of Cav1.2 exon 8 and 8a showing a high level of sequence homology (Genbank accession numbers: NM_001255999.2, NM_001256000.2). **c.** Expression levels of Cav1.2 exon 8 and 8a in adrenal medullae of WT (n= 2 mice) and TS2-neo (n= 3 mice) mice using quantitative RT-PCR. One-way ANOVA followed by Holm-Sidak post-test; ***p<0.001.

Figure 3. *Voltage-dependence of L-type currents and cell capacitance are altered in TS2-neo mutated MCCs.* **a**. Two sets of pharmacologically isolated L-type Ca^{2+} currents evoked by depolarizing pulses of 20 ms from −40 to +20 mV in step of 10 mV from a WT and TS2-neo MCC. **b**. Overlapped L-type Ca^{2+} currents recorded from a WT MCC at +20 mV in control condition (black trace) and after acute application of 15 µM nifedipine (red trace), which fully blocks the Ca^{2+} current. **c.** Normalized *I-V* relationship of peak L-type Ca^{2+} currents recorded during step depolarizations of 20 ms at the indicated potentials from V_h = -70 mV for WT (black squares) and TS2-neo MCCs (red dots) (n= 17 WT cells in 6 cultures and n= 17 TS2-neo cells in 6 cultures; *p< 0.05). TS-2 neo L-type currents activation (red curve) is leftward shifted with respect to WT (black curve) (**p< 0.01; *p< 0.05, unpaired t-test). **d.** Normalized L-type Ca^{2+} channel conductance, *gCa(V),* for WT (black line) and TS2-neo MCCs (red line) calculated from *gCa(V)=ICa/(V- ECa)* with *ECa*= +60 mV in which is evident the same negative shift of the *I-V*

relationship. The two continuous curves are the results of the fit with two Boltzmann equations with half-maximal values $V_{½}$ (in mV) and slope factors *k* (in mV) obtained from the fit: −0.7 mV and 10.7 mV (WT; black curve) and −5.8 mV and 10.5 mV (TS2-neo; red curve) (n= 17 WT cells in 6 cultures and n= 17 TS2-neo cells in 6 cultures). **e**. Mean peak L-type currents, membrane capacitance and current density from WT (black bars) and TS2-neo MCCs (red bars). TS2-neo mutation increases the membrane capacitance either determined from the pool of cells used to obtain *gCa(V)* (n= 19 WT cells from 6 cultures and n= 20 TS2-neo cells from 6 cultures) or from a larger pool of cells used for other experiments (n= 65 WT cells in 12 cultures and n= 59 TS2-neo cells in 12 cultures). The capacitance increase reduces the L-type Ca^{2+} currents density of TS2-neo MCCs.

Figure 4. ***L-type channel inactivation is slower and less complete in TS2-neo mutated MCCs*****. a.** Mean normalized L-type Ca^{2+} currents evoked by 1 s depolarizing pulses to +10 mV (*left*) for WT (n= 11 cells in 4 cultures; black trace) and TS2-neo MCCs (n= 11 cells in 4 cultures; red trace). In the two mean traces are evident the fast (CDI) and slowly inactivating (VDI) components of L-type Ca^{2+} currents. *Right:* averages of the percentage of L-type Ca^{2+} currents persisting after 1 s depolarization to +10 mV from WT (black) and TS2-neo (red) MCCs (**p< 0.01). The two continuous curves of different colour drawn on top of the traces are the result of a curve fit with a double exponential function (see text). **b.** Same normalized mean traces as described in **a,** with Ba^{2+} replacing Ca^{2+} as charge carrier (n= 11 WT cells in 4 cultures and n=9 for TS2-neo cells in 4 cultures). The TS2-neo mutation slows the VDI of L-type currents. **c.** *Top:* pulse protocol used to determine the voltage-dependence of CDI of isolated L-type currents for WT (black traces) and TS2-neo MCCs (red traces). *Bottom:* Mean normalized values for CDI vs. voltage for WT (black line) and TS2-neo MCCs (red line). Data represents the fraction of the peak current remaining after 100 ms upon depolarization with Ca^{2+}. TS2-neo isolated L-type Ca^{2+} currents are less inactivating, especially at potentials >+40 mV (n= 7 WT cells in 2 cultures and n= 7 TS2-neo cells in 2 cultures ; *p<0.05).

Figure 5. ***Steady-state inactivation of L-type current is leftward shifted and "window current" is markedly increased in TS2-neo mutated MCCs. a.*** Pulse protocol used to determine the steady state inactivation (SSI) of isolated L-type Ca^{2+} currents in MCCs. **b.** Representative L-type Ca^{2+} currents recorded during test protocols P_1 and P_2 at +20 mV, separated by 5 s

depolarization to a pre-determined potential in WT (black traces) and TS2-neo MCCs (red traces). **c.** Steady-state inactivation curves for WT (black squares) and TS2-neo (red dots) MCCs. The two continuous curves are the results of a curve fit with two Boltzmann equations with $V_{½}$ and slope factors *k*: −20.8 mV and 7.4 mV (n= 11 WT cells in 4 cultures; black curve) and −29.5 mV and 8.2 mV (n= 12 TS2-neo cells in 4 cultures; red curve). **d.** Window Ca^{2+} current (*Iw*) calculated from *SSI(V)* and *gCa(V)*. *Iw* is obtained by multiplying the probability of channel openin *po(V)* by the driving force *(V-ECa)* with *ECa*= +60 mV (continuous curves in bottom panel). The two *po(V)* curves are obtained by multiplying *SSI(V)* by *gCa(V)* (dotted curves on top panel). Notice the increased amplitude of *Iw* between -70 and -40 mV (shadowed area).

Figure 6. ***TS2-neo mutation increases the percentage of cells undergoing burst firing and alters the waveform of spontaneous repetitive action potentials. a***. Mean V_{rest} in WT (n= 14 cells in 6 cultures, black bar) and TS2-neo MCCs (n= 19 cells in 6 cultures, red bar). **b**. Proportions of silent, tonically or burst firing MCCs in WT (n= 20 cells in 6 cultures; black bars) and TS2-neo MCCs (n= 20 cells in 6 cultures, red bars). The TS2-neo mutation switches MCCs spontaneous activity in to bursts (*< 0.05; Chi square test). **c**. Mean frequency, peak amplitude, half-width and antipeak amplitude during spontaneous tonic firing in WT (n= 11 cells in 6 cultures, black bars) and TS2-neo MCCs (n= 5 cells in 6 cultures, red bars). Mean values were obtained by averaging single values from six consecutive spikes during the spontaneous activity (*p< 0.05; unpaired t-test). **d**, **e**. Representative traces of spontaneously repetitive AP firing in a WT (*d*) and a TS2-neo MCC (*e*). Details of the firing activity are shown in an expanded time scale in the grey inset below. **f**. Overlap of mean WT (black) and TS2-neo APs (red). Averaged traces were obtained from six consecutive APs during the trains. **g**. Phase-plane plot (*dV/dt* vs. *V*) of six consecutive APs from WT (black traces) and TS2-neo MCCs (red traces). *Inset*: Mean maximal *dV/dt* as a measure of maximal rate of rise of APs from n= 5 WT cells in 5 cultures and n= 7 TS2-neo cells in 5 cultures (**p< 0.01, unpaired t-test).

Figure 7. The waveform of s*pontaneous burst firing is markedly altered in TS2-neo mutated cells. a-c.* Representative traces of spontaneous burst firing in WT (***a***) and TS2-neo MCCs (***b, c***). TS2-neo burst activity at low- (***b***) and high-frequency (***c***) is markedly undershoot respect to WT. Grey windows show expanded intervals of bursts at the same time scale. The expanded burst (red trace in the right-inset) shows how was estimated the number of event, the mean plateau

phase and bursts duration. The mean plateau amplitude was determined as the half-amplitude of the slow repolarization that was assumed to increase linearly from the first to the last spike. Burst duration was calculated from the fast rising of the first AP to the end of the fast repolarization of the last AP, just before the onset of the following slower depolarization. **d.** Means of number of events during burst (*left*), 1st and last peak amplitude *(right*) for WT (n= 4 cells in 3 cultures, black bars) and TS2-neo MCCs (n= 7 cells in 5 cultures, red bars) (**p< 0.01, *p< 0.05; unpaired t-test). TS2-neo mutation drastically reduces the number of events during burst and shifts to negative or more negative values the 1st and the last peak amplitude. **e.** Comparison of mean plateau amplitude, burst duration and number of burst per minute between WT (n= 4 cells in 3 cultures, black bars) and TS2-neo MCCs (n= 7 cells in 5 cultures, red bars). The burst parameters are comparable between the two groups.

Figure 8. ***Nav channel density is markedly attenuated and voltage-dependent steady-state inactivation of Nav channels is leftward shifted in TS2-neo mutated MCCs. a.*** Isolated Na^+ currents evoked by depolarizing pulses of 10 ms from −50 to +50 mV in step of 10 mV from WT (black traces) and TS2-neo MCCs (red traces). **b.** Mean values of peak Nav currents at 0 mV, membrane capacitance and currents density from WT (n= 21 cells in 4 cultures, black bars) and TS2-neo MCCs (n= 21 cells in 4 cultures, red bars; *p< 0.05, unpaired t-test). The TS2-neo mutation significantly increases the membrane capacitance thus reducing Nav currents density. **c,d.** *I–V* relationship and normalized conductance for Nav current densities measured at V_h = -70 mV for WT (n= 11 cells in 3 cultures; black traces) and TS2-neo MCCs (n= 13 cells in 3 cultures; red traces). ***e-f.*** Mean normalized values for fast and slow Nav channel inactivation from WT (n= 11 cells in 4 cultures; black traces) and TS2-neo MCCs (n= 13 cells in 4 cultures; red traces).

Figure 9. ***Voltage- and Ca^{2+}-dependence of BK channels is not affected in TS2-neo mutated MCCs.*** **a.** *Top***.** Pulse protocol used to evaluate the voltage-dependence of BK currents. **Bottom**. Representative total K^+ currents (BK + K_V) (*top*), during application of the BK channel blocker paxilline (1 µM, *middl*e) and subtraction of total from paxilline-resistant currents (*bottom*). WT currents are shown to the left while TS2-neo currents to the right. **b.** Conductance of BK channels obtained by a sigmoidal fit for WT (n= 8 cells in 3 cultures black trace) and TS2-neo currents (n= 10 cells in 3 cultures,red traces). The mutation leads to a left shift of the Boltzmann curve. **c.** *Top*. Pulse protocol used to evaluate the Ca^{2+}-dependence of BK currents. *Bottom*. BK

and Kv currents measured in WT (*left*) and TS2-neo MCCs (*right*). The BK current amplitude (black arrow, IBK) is obtained by subtraction of the K_V current (measured at +120 mV; red arrow, I_{Kv}) to the total K^+ current. **d.** Normalized I_{BK} currents versus voltage for WT (n= 8 cells in 3 cultures, black trace) and TS2-neo MCCs (n= 10 cells in 3 cultures, red trace). Notice the "bell-shaped" curve corresponding to the Ca^{2+}-dependence of BK currents. ***Right*.** Mean BK current amplitude measured at +120 mV, for WT (black) and TS2-neo cells (red). **e.** *Left*. Mean Kv current amplitudes in WT (black) and TS2-neo cells (red). *Right*. Mean Kv current amplitude measured at +120 mV, for WT (black n= 8 cells in 4 cultures) and TS2-neo cells (n= 10 cells in 4 cultures red).

Figure 10. ***TEM images, biochemical assays of mitochondrial function, TUNEL and DAPI tests in WT and TS2-neo MCCs*** a. *Top*: Electron micrographs showing WT (left) and TS2-neo MCCs (right) at low magnification. TS2-neo MCCs show an altered nuclear (Nu) and cytoplasmic morphology, with extensive vacuolization (vac) and fewer intracellular organelles. *Bottom*: Higher magnification corresponding to the boxed regions, showing the abnormal morphology of mitochondria (mit) and large dense core granules (LDCG, white arrows) in TS2-neo MCCs. Specifically, in mutated cells mitochondria have fewer cristae whereas LDCGs show an evident perigranular swelling. Scale bars: *top* images 2 µm; *bottom* images 500 nm. **b.** *Top.* Histogram illustrating the cell area distribution in WT (grey and black bars) and TS2-neo MCCs (light- and dark-red bars). Note the clear separation with significantly different means. *Bottom*: Mean cell area (μm^2) in TS2-neo (red bars; n= 50 cells) and WT MCCs (black bars; n= 50 cells; Mann Whitney test; ****p< 0.0001). **c.** The rate of electron flux from complex I to complex III was evaluated in isolated MCCs (left panel). The mitochondrial membrane potential was assessed by the JC-1 staining method. The percentage of green versus red mitochondria was considered a marker of mitochondrial depolarization and permeability transition (middle panel). ATP was measured in duplicates in the mitochondrial extracts by a chemiluminescence-based assay (right panel). All measurements were performed in duplicates and data are presented as means ± SD (n= 6 animals/group; ***p< 0.001). **d.** Low-magnification micrographs of adrenal medulla gland sections obtained from WT and TS2-neo mice. All sections were decorated by TUNEL (red) and DAPI (grey) to reveal apoptotic cells. Scale bar: 50 µm. The yellow arrows in the right panel indicate two rare TUNEL positive mutated cells.

Figure 11. ***Ca^{2+}-dependent secretion is attenuated in TS2-neo mutated MCCs.***

a. Representative traces of depolarization-evoked secretion in WT (black traces, *left*) and TS2-neo MCCs (red traces, *right*). It is visible the capacitance increase (*DC*, *top*) and the Ca^{2+} current (*bottom*) recorded during a step depolarization to +10 mV (*upper* panel) or 0 mV (*lower* panel). **b**. Mean capacitance changes *DC* (left) and mean quantity of charge *Q* (right) associated to the depolarizing pulse measured in WT (n= 12 cells in 6 cultures, black bars) and TS2-neo MCCs (n= 16 cells in 7 cultures, red bars) both at +10 mV and measured in WT (n= 11 cells in 6 cultures, black bars) and TS2-neo MCCs (n= 13 cells in 7 cultures, red bars) at 0 mV. DC is reduced at both voltages in mutated MCCs with respect to WT (**p<0.01, unpaired t-test). **c.** Ca^{2+}-dependence of the exocytosis determined by plotting *DC* (fF) vs the corresponding Ca^{2+}-charge density *Q* (pC/pF). The slope of the linear regression for WT (filled squares, black line) is statistically different from the TS2-neo one (see text) (triangles, red line; **p< 0.01, unpaired t-test). **d.** Representative traces of the double pulse protocol used to estimate the maximal size of the RRP in WT (left, black traces) and TS2-neo MCCs (right, red traces). Upper limit of the RRP estimated from $B_{max}= (\Delta C_1 + \Delta C_2)/(1 - (\Delta C_2/\Delta C_1)^2)$, where ΔC_1 and ΔC_2 are the capacitance increases associated to the consecutive depolarizing pulses. **e.** Mean B_{max} (RRP, left plot) and probability of release (*Pr*; right plot) for WT (n= 8 cells in 3 cultures, black bar) and mutated MCCs (n= 8 in 5 cultures, red bar). *Pr* is statistically smaller in TS2-neo MCCs (*p< 0.05, unpaired t-test).

Figure 12 - ***Spontaneous repetitive firing recorded in current-clamp from two representative WT MCCs***. WT MCCs were bathed in Tyrode solution (2 mM Ca^{2+}) and recorded in current-clamp mode with 0 current injection. Verapamil at two different concentrations (15 µM and 5 µM) was applied during the period indicated by the horizontal bars. Notice the marked resting potential hyperpolarization and firing block during the application of the Ca channel blocker.

Figure 13. ***Overnight incubations of the L-type channel blockers verapamil and nifedipine rescues the normal spontaneous firing in TS2-neo mutated cells. a.*** Representative burst firing from TS2-neo MCCs overnight incubated with 15 µM verapamil. The pharmacological treatment completely recover a normal burst activity. **b.** *Top:* Mean values for 1st and last peak amplitude during burst in WT (n= 4 cells in 3 cultures, black bars), TS2-neo (n= 7 cells in 5 cultures, red bars) and TS2-neo + verapamil 15 µM overnight treated MCCs (n= 4 cells in 3 cultures, grey bars). Verapamil incubation rescues the overshoot of 1st peak amplitude and makes less negative the last peak amplitude (**p< 0.01, p*< 0.05, one-way ANOVA followed by Holm-Sidak

post-test). *Bottom:* mean number of events during burst (*left*) and mean plateau amplitude (*right*) in WT (black bars), TS2-neo (red bars) and TS2-neo + verapamil 15 µM (grey bars). Verapamil treatment rescues values comparable to WT. **c.** Repetitive firing recorded from a representative TS2-neo MCCs overnight incubated with 0.3 µM nifedipine. Tonic firing is more evident in the last part of the recording, after the manual hyperpolarization induced by passing −5 pA to hold V_{rest} to −70 mV. This procedure was not used routinely and did not bias the estimate of maximal AP amplitude that was always estimated soon after the initial track of the recording. **d.** Proportions of silent, tonically or burst firing MCCs in WT (n= 20 cells in 6 cultures; black bars), TS2-neo MCCs (n= 20 cells in 6 cultures, red bars) and TS2-neo + 0.3µM nifedipine treated MCCs (n= 23 cells in 6 cultures, grey bars) (*<0.05, **p< 0.01; Chi square test). **e.** *Top left:* single APs obtained from WT (black), TS2-neo (red) and TS2-neo + 0.3µM nifedipine treated MCCs (grey). *Top right and bottom:* mean peak amplitude, antipeak amplitude and half-width for WT (n=14 cells in 6 cultures, black bars), TS2-neo (n= 10 cells in 6 cultures , red bars) and TS2-neo + 0.3 µM nifedipine treated MCC (n= 16 cells in 7 cultures, grey bars; **p< 0.01, p*< 0.05, one-way ANOVA followed by Holm-Sidak post-test).

Figure 14. ***Overnight incubations and acute application of L-type channel blockers nifedipine abolishes the spontaneous firing of WT MCCs. a.*** Representative trace with no evident resting activity recorded from a WT MCCs overnight incubated with 0.3 µM nifedipine (n= 14 cells in 2 cultures). The DHP treatment completely abolishes the spontaneous firing activity. Single APs were evident following pre-hyperpolarizations to ~-70 mV passing negative current. ***b1.*** Representative trace recorded from a TS2-mutated MCC in which is evident that bath application of 3 µM nifedipine fully blocks the spontaneous firing activity (n= 5 cells in 2 cultures). ***b2.*** Representative trace recorded before, during and after acute application of 0.3 µM nifedipine on a TS2-mutated MCC. Also at this low concentration the drug completely block the spontaneous firing activity (n= 6 total cells in 3 cultures).

Figure 15. ***Overnight incubations with the L-type channel blocker nifedipine rescues the density and SSI of Nav channels as well as Ca^{2+}-dependent secretion in TS2-neo MCCs. a.*** Phase-plane plot (*dV/dt* vs. *V*) of six consecutive APs from WT (black traces), TS2-neo MCCs (red traces) and TS2-neo + 0.3 µM nifedipine (blue traces). *Right:* maximum values of *dV/dt* attained in the phase-plane plot calculated on the first AP. TS2-neo nifedipine-treated MCCs (n= 16 in 7

cultures) has values comparable to WT cells (n= 10 cells in 5 cultures) and significantly higher than TS2-neo untreated cells (n= 7 cells in 5 cultures, ~~*p<0.05 and~~ **p< 0.001; one-way ANOVA followed by Holm-Sidak post-test). ***b.*** Mean values of Na_V peak currents (at -10 or 0 mV), membrane capacitance and density of currents in TS2-neo and TS2-neo + 0.3 µM nifedipine MCCs. The DHP treatment partially recovers the Na_V channels currents amplitude and increases by ~30% the current density (n= 13 TS2-neo cells in 5 cultures and n= 11 TS2-neo +nife cells in 5 cultures). ***c.*** Normalized mean Na_V currents evoked by depolarizing pulses of 10 ms to -10 mV from −70 mF. Na_V currents were recorded and averaged from n= 4 from TS2-neo cells (red trace) and n= 4 TS2-neo + 0.3 µM nifedipine cells (blue trace), and fully blocked by 300 nM TTX. ***d.*** *Normalized I–V* relationship of Na_V current measured at V_h = -70 mV for TS2-neo (n= 13 cells in 5 cultures; red traces) and TS2-neo + 0.3 µM nifedipine MCCs (n= 13 cells in 5 cultures; blue traces). ***e.*** Mean normalized values for steady-state Na_V channel inactivation for TS2-neo (n= 13 cells in 5 cultures; red traces) and TS2-neo + 0.3µM nifedipine MCCs (n= 13 cells in 5 cultures; blue traces). ***f.*** Representative traces of depolarization-evoked secretion in TS2-neo (red traces, *left*) and TS2-neo + 0.3 µM nifedipine MCCs (blue traces, *right*). It is visible the capacitance increase (ΔC, *top*) and the Ca^{2+} current (*bottom*) recorded during a step depolarization to +10 mV (*upper* panel) or 0 mV (*lower* panel). ***g.*** Mean capacitance changes ΔC (left) and mean quantity of charge Q (right) associated to the depolarizing pulse measured in TS2-neo (n= 16 cells in 7 cultures, red bars) and TS2-neo +0.3 µM nifedipine MCCs (n= 9 cells in 6 cultures, blue bars) at +10 mV and measured in TS2-neo (n= 13 cells in 7 cultures , red bars) and TS2-neo + 0.3 µM nifedipine MCCs (n= 9 cells in 6 cultures, blue bars) at 0 mV. ΔC is recovered at both voltages in mutated MCCs treated with 0.3 µM nifedipine with respect to untreated MCCs (**p< 0.01, one-way ANOVA followed by Holm-Sidak post-test). ***h.*** Ca^{2+}-dependence of the exocytosis determined by plotting ΔC (fF) vs the corresponding Ca^{2+}-charge density Q (pC/pF). The slope of the linear regression for TS2-neo (triangles, red line) is statistically different from the TS2-neo + 0.3 µM nifedipine one (see text) (empty squares, blue line, **p< 0.01, unpaired t-test).

a

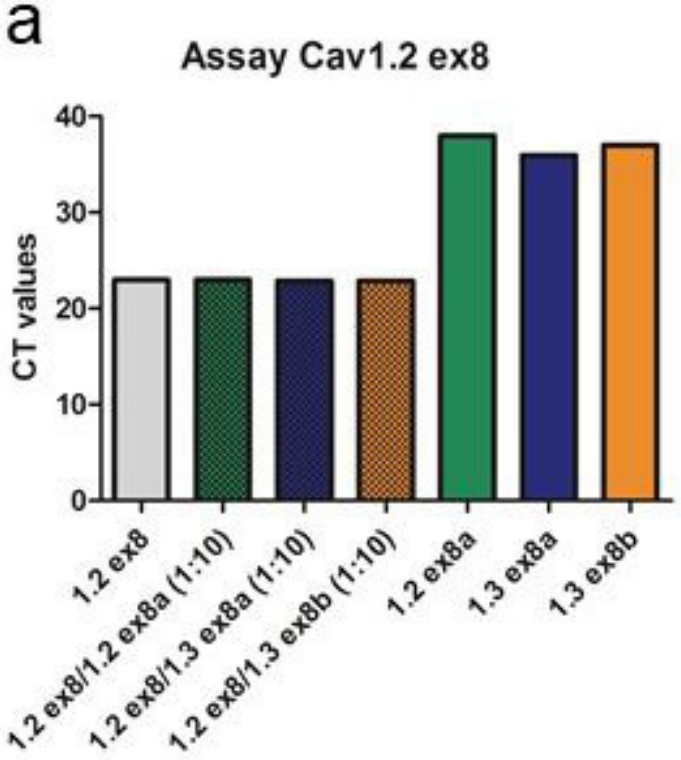
Assay Cav1.2 ex8
CT values
40
30
20
10
0
1.2 ex8
1.2 ex8/1.2 ex8a (1:10)
1.2 ex8/1.2 ex8a (1:10)
1.2 ex8/1.3 ex8a (1:10)
1.2 ex8/1.3 ex8b (1:10)
1.2 ex8a
1.3 ex8a
1.3 ex8b

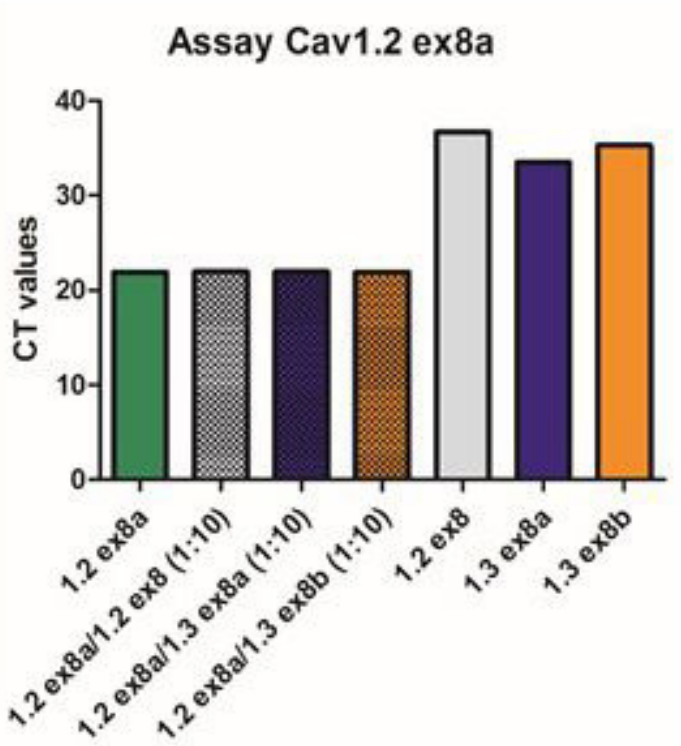
Assay Cav1.2 ex8a
CT values
40
30
20
10
0
1.2 ex8a
1.2 ex8a/1.2 ex8 (1:10)
1.2 ex8a/1.3 ex8a (1:10)
1.2 ex8a/1.3 ex8b (1:10)
1.2 ex8
1.3 ex8a
1.3 ex8b

b

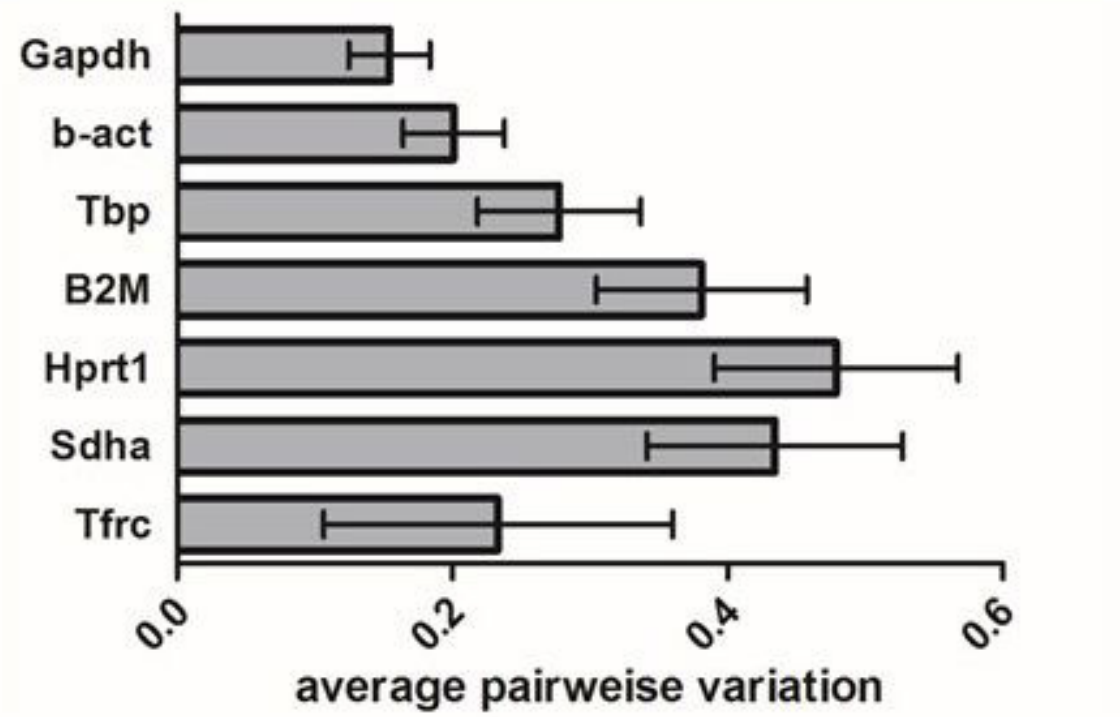
Gapdh
b-act
Tbp
B2M
Hprt1
Sdha
Tfrc
0.0
0.2
0.4
0.6
average pairweise variation

Fig. 1

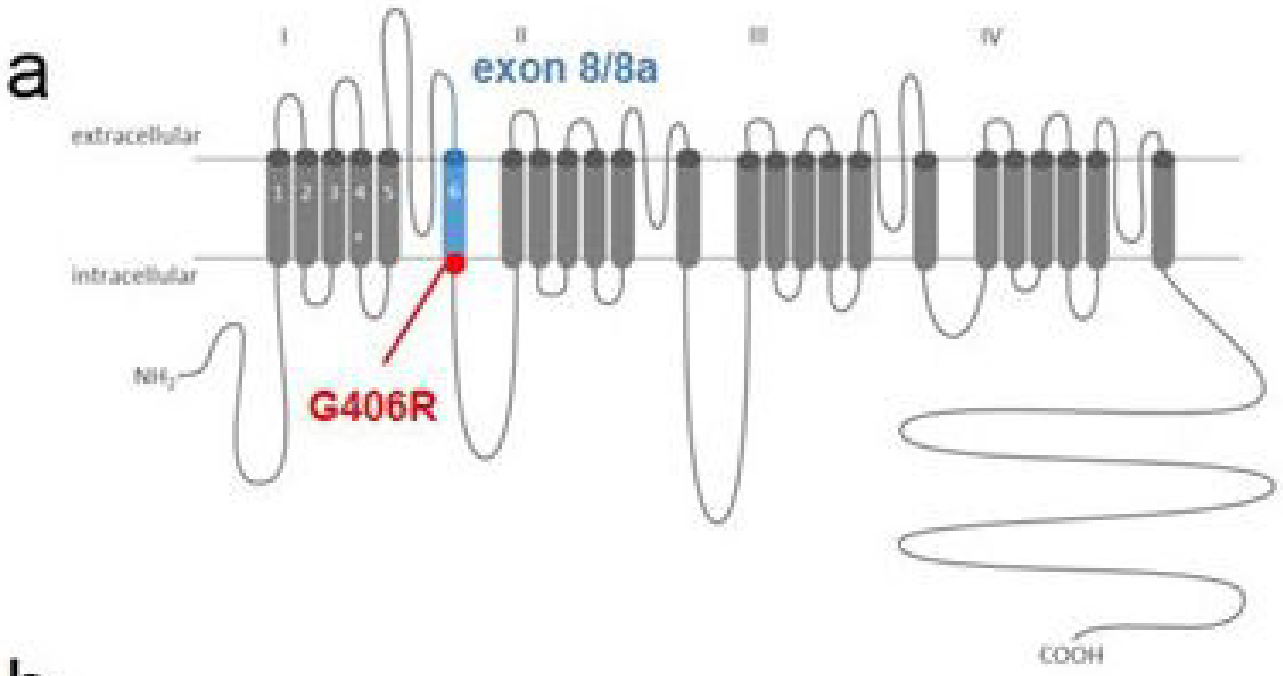

b

R

Cav1.2 ex8 MQDAMGYELPWVYFVSLVIFGSFFVLNLVLGVLSG

Cav1.2 ex8a VNDAVGRDWPWIYFVTLIIIGSFFVLNLVLGVLSG

IS6

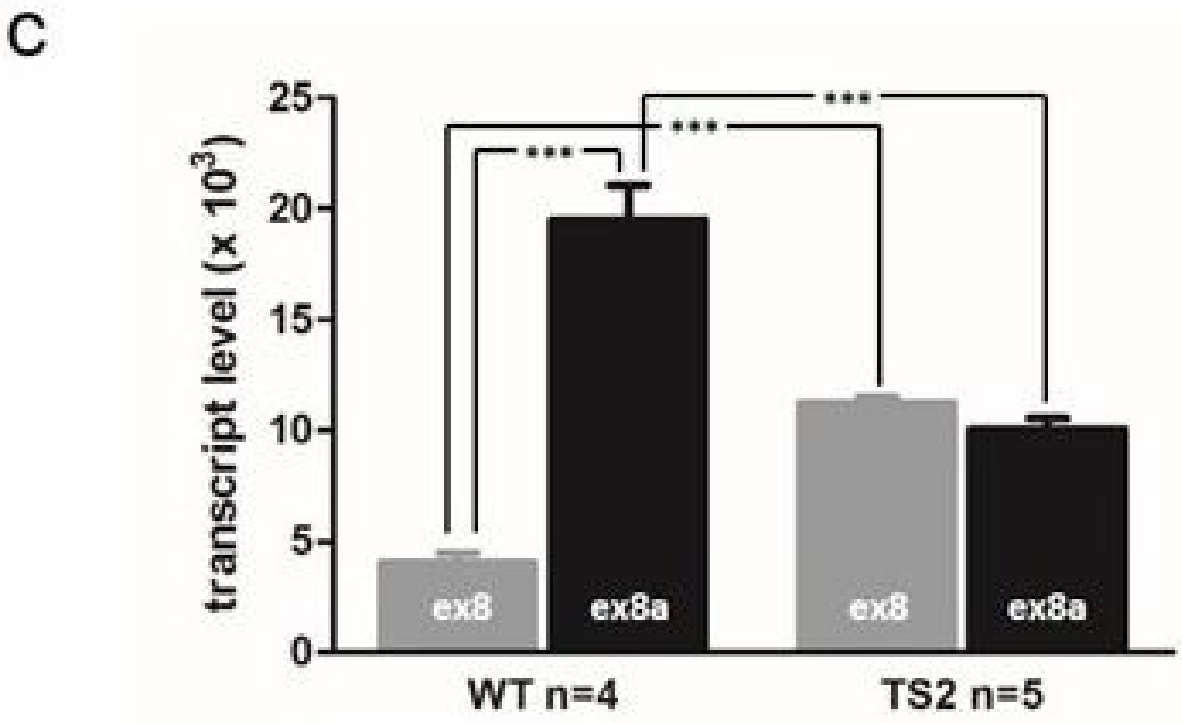

Fig. 2

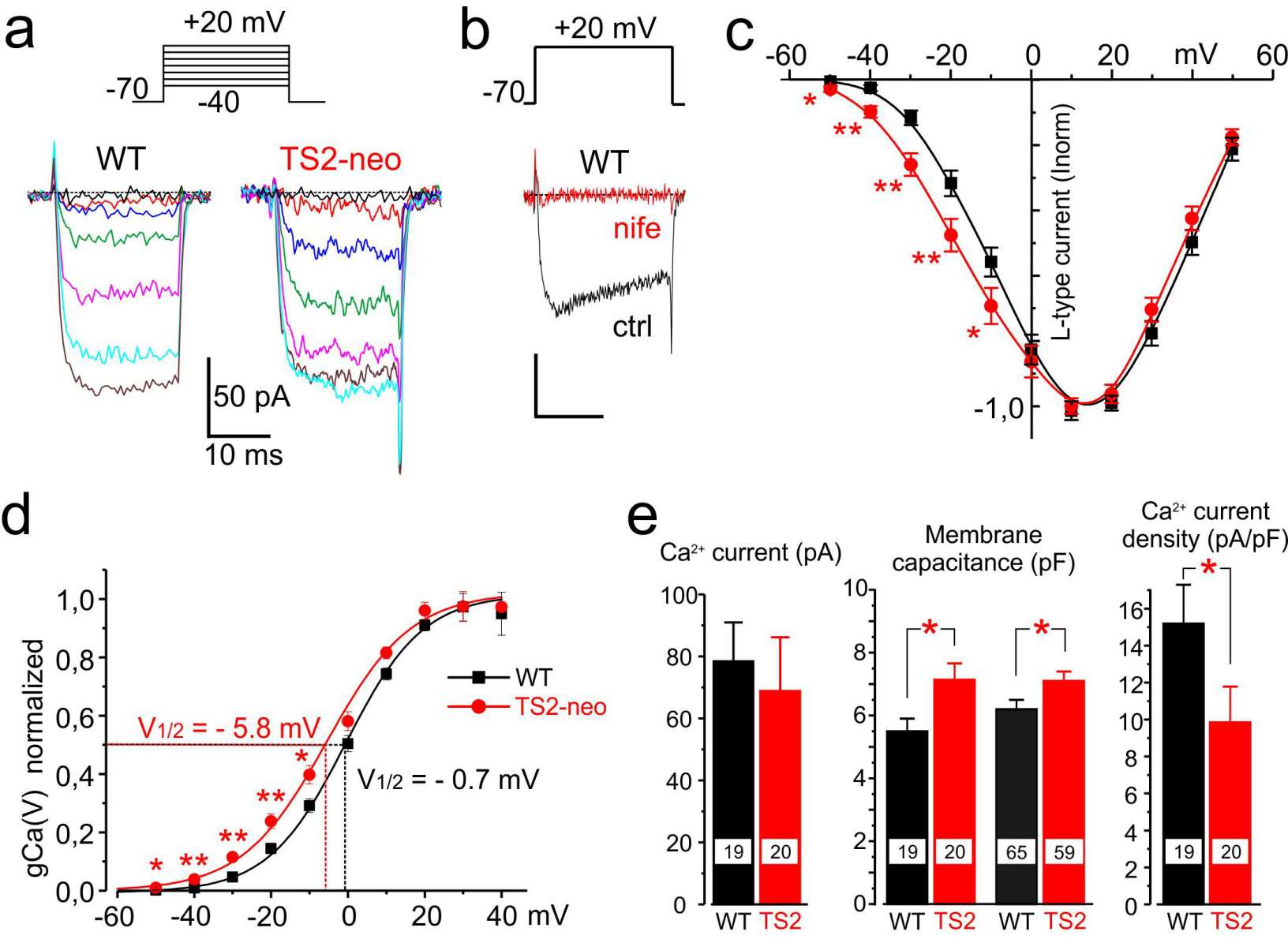
a
+20 mV
-70
-40
WT
TS2-neo
50 pA
10 ms
b
+20 mV
-70
WT
nife
ctrl
c
-60
-40
-20
0
20
mV
60
L-type current (Inorm)
-1,0
d
gCa(V) normalized
1,0
0,8
0,6
0,4
0,2
0,0
-60
-40
-20
0
20
40 mV
WT
TS2-neo
V1/2 = - 5.8 mV
V1/2 = - 0.7 mV
e
Ca2+ current (pA)
Membrane capacitance (pF)
Ca2+ current density (pA/pF)
WT TS2
19
20
65
59

Fig. 3

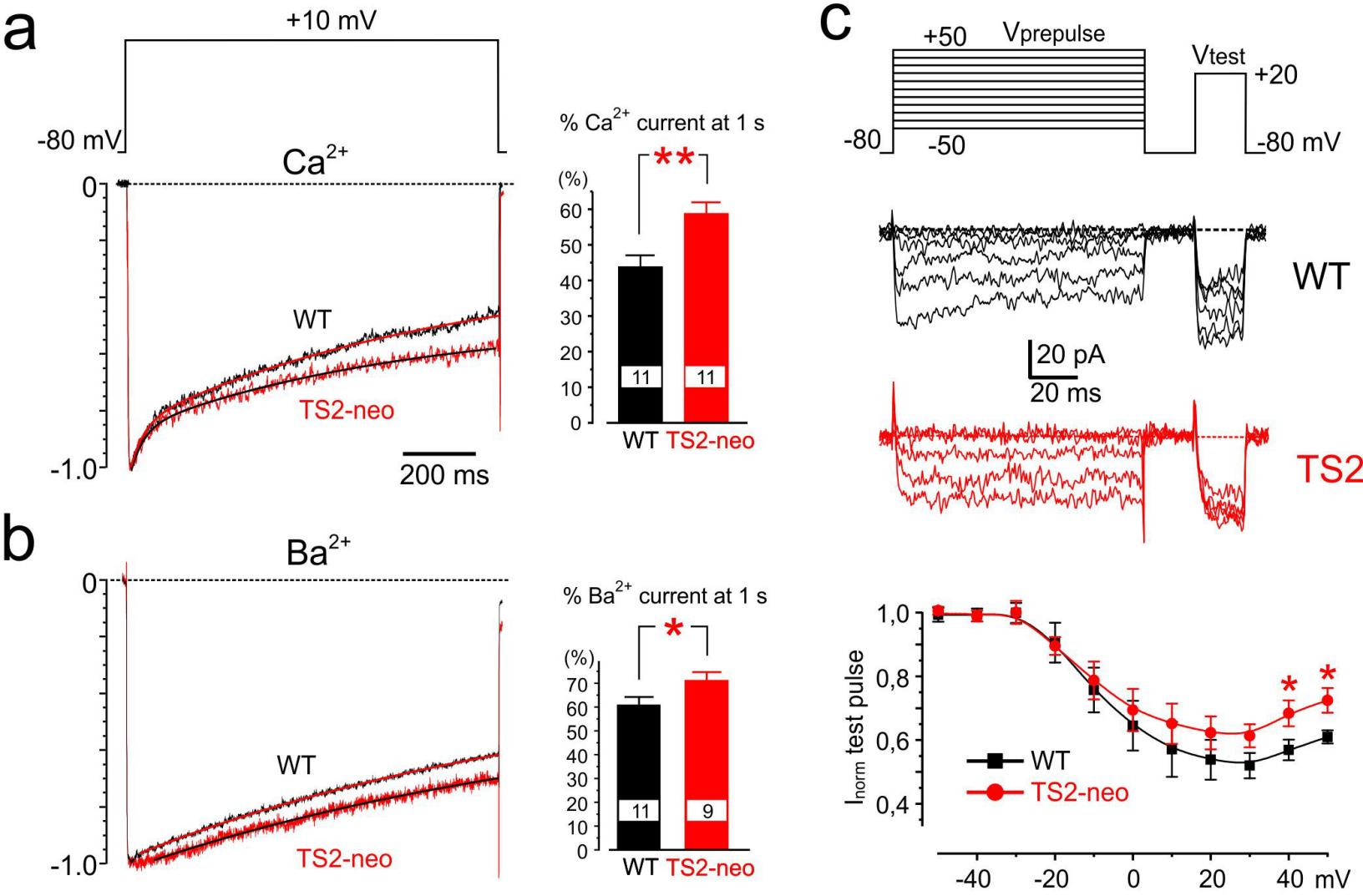
a
+10 mV
-80 mV
Ca2+
0
-1.0
WT
TS2-neo
200 ms
% Ca2+ current at 1 s
**
(%)
60
50
40
30
20
10
0
11
11
WT TS2-neo
b
Ba2+
0
-1.0
WT
TS2-neo
% Ba2+ current at 1 s
*
(%)
70
60
50
40
30
20
10
0
11
9
WT TS2-neo
c
+50
Vprepulse
Vtest
+20
-80
-50
-80 mV
WT
20 pA
20 ms
TS2
1,0
0,8
0,6
0,4
Inorm test pulse
WT
TS2-neo
-40
-20
0
20
40 mV

Fig. 4

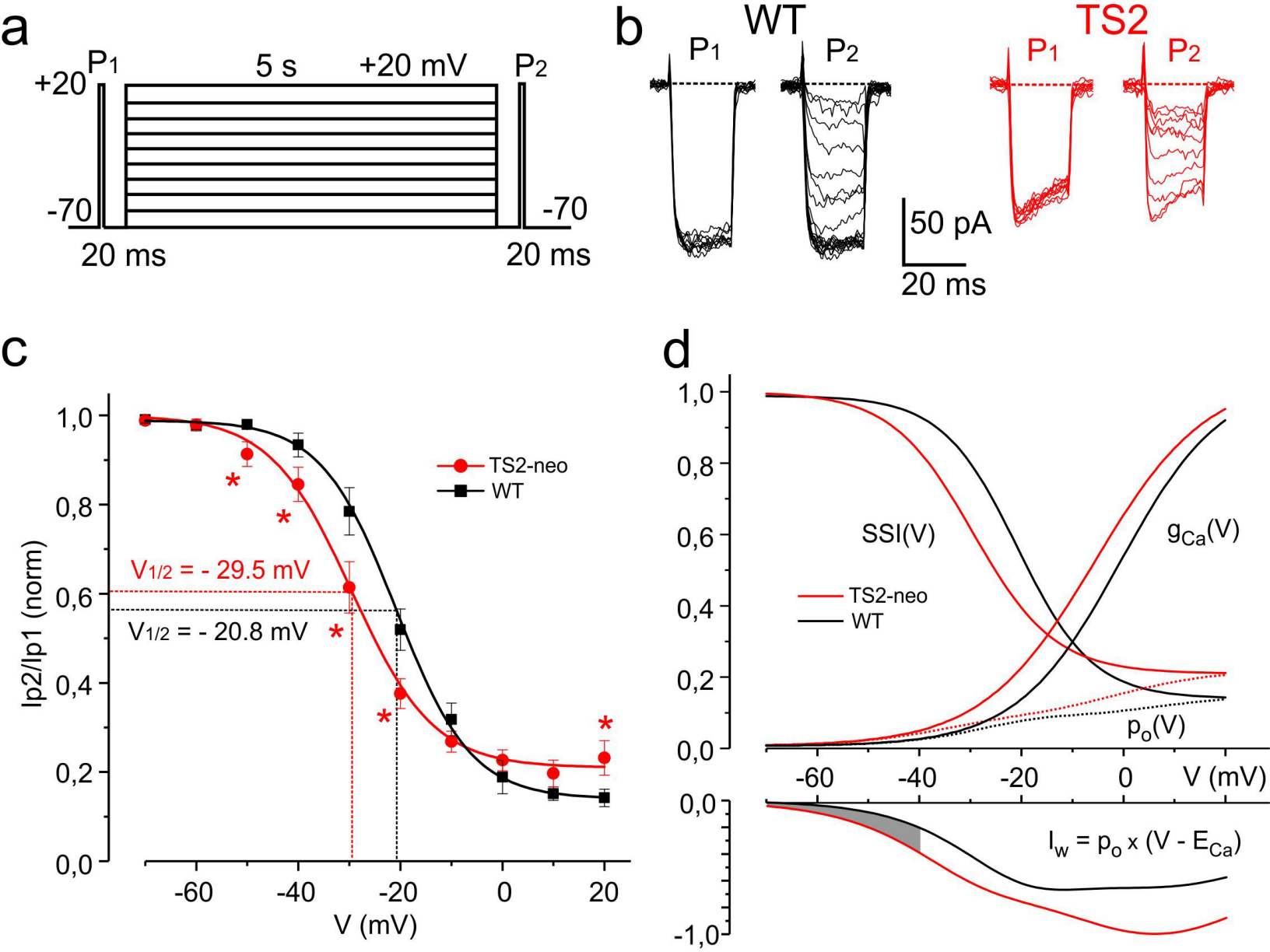
a
P1
5 s
+20 mV
P2
+20
-70
-70
20 ms
20 ms
b
WT
TS2
P1
P2
P1
P2
50 pA
20 ms
c
1,0
0,8
0,6
0,4
0,2
0,0
Ip2/Ip1 (norm)
TS2-neo
WT
V1/2 = - 29.5 mV
V1/2 = - 20.8 mV
-60
-40
-20
0
20
V (mV)
d
1,0
0,8
0,6
0,4
0,2
0,0
SSI(V)
gCa(V)
TS2-neo
WT
po(V)
-60
-40
-20
0
V (mV)
0,0
-1,0
Iw = po x (V - ECa)

Fig. 5

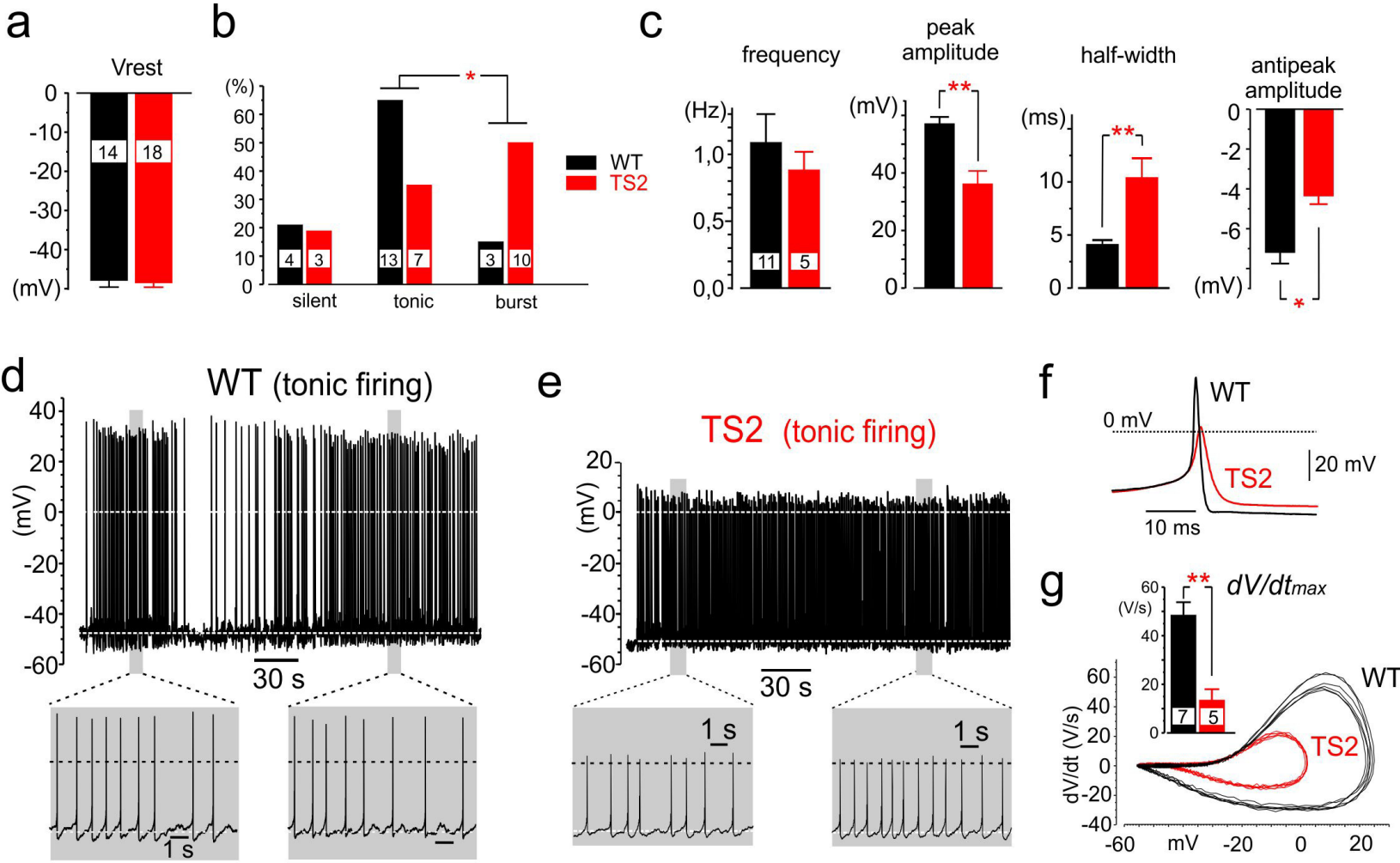
a
Vrest
0
-10
-20
-30
-40
(mV)
14
18
b
(%)
60
50
40
30
20
10
0
*
4
3
13
7
3
10
silent
tonic
burst
WT
TS2
c
frequency
(Hz)
1,0
0,5
0,0
11
5
peak amplitude
(mV)
40
20
0
**
half-width
(ms)
10
5
0
**
antipeak amplitude
0
-2
-4
-6
(mV)
*
d
WT (tonic firing)
40
20
0
-20
-40
-60
(mV)
30 s
1 s
e
TS2 (tonic firing)
20
0
-20
-40
-60
(mV)
30 s
1 s
1 s
f
WT
0 mV
TS2
20 mV
10 ms
g
dV/dtmax
60
(V/s)
40
20
0
**
7
5
WT
TS2
60
40
20
0
-20
-40
dV/dt (V/s)
-60
mV
-20
0
20

Fig. 6

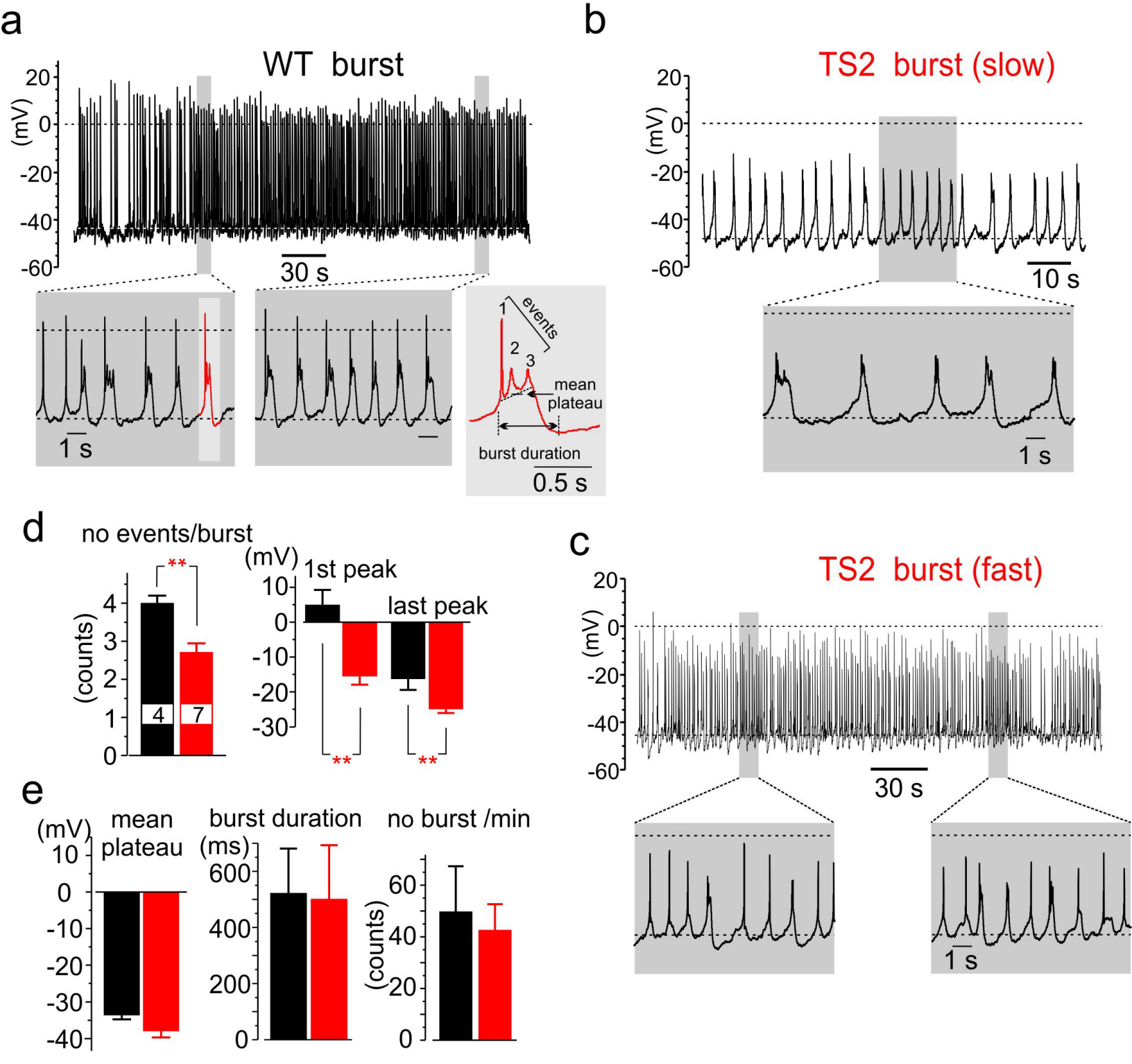
a
WT burst
20
0
-20
-40
-60
(mV)
30 s
1 s
1
events
2
3
mean
plateau
burst duration
0.5 s
b
TS2 burst (slow)
10 s
1 s
c
TS2 burst (fast)
30 s
1 s
d
no events/burst
(counts)
**
4
7
(mV)
1st peak
last peak
e
mean
plateau
burst duration
(ms)
no burst /min
(counts)

Fig. 7

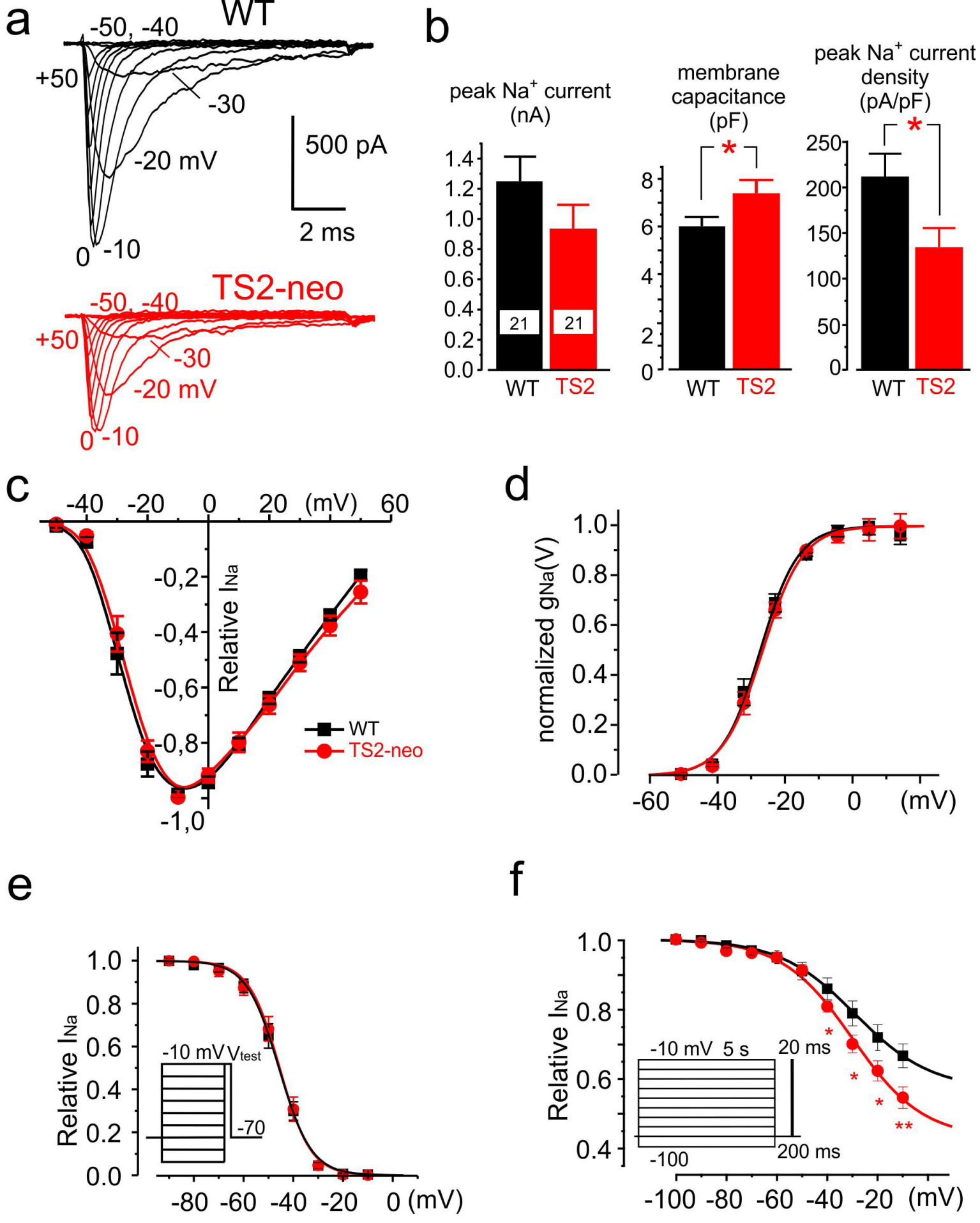
a
WT
-50, -40
+50
-30
-20 mV
500 pA
2 ms
0
-10
TS2-neo
-50, -40
+50
-30
-20 mV
0
-10
b
peak Na+ current (nA)
1.4
1.2
1.0
0.8
0.6
0.4
0.2
0.0
21
21
WT
TS2
membrane capacitance (pF)
8
6
4
2
0
*
WT
TS2
peak Na+ current density (pA/pF)
250
200
150
100
50
0
*
WT
TS2
c
-40
-20
0
20
(mV)
60
Relative INa
-0,2
-0,4
-0,6
-0,8
-1,0
WT
TS2-neo
d
normalized gNa(V)
1.0
0.8
0.6
0.4
0.2
0.0
-60
-40
-20
0
(mV)
e
Relative INa
1.0
0.8
0.6
0.4
0.2
0.0
-10 mV Vtest
-70
-80
-60
-40
-20
0 (mV)
f
Relative INa
1.0
0.8
0.6
0.4
-10 mV 5 s
20 ms
200 ms
-100
*
*
*
**
-100
-80
-60
-40
-20
(mV)

Fig. 8

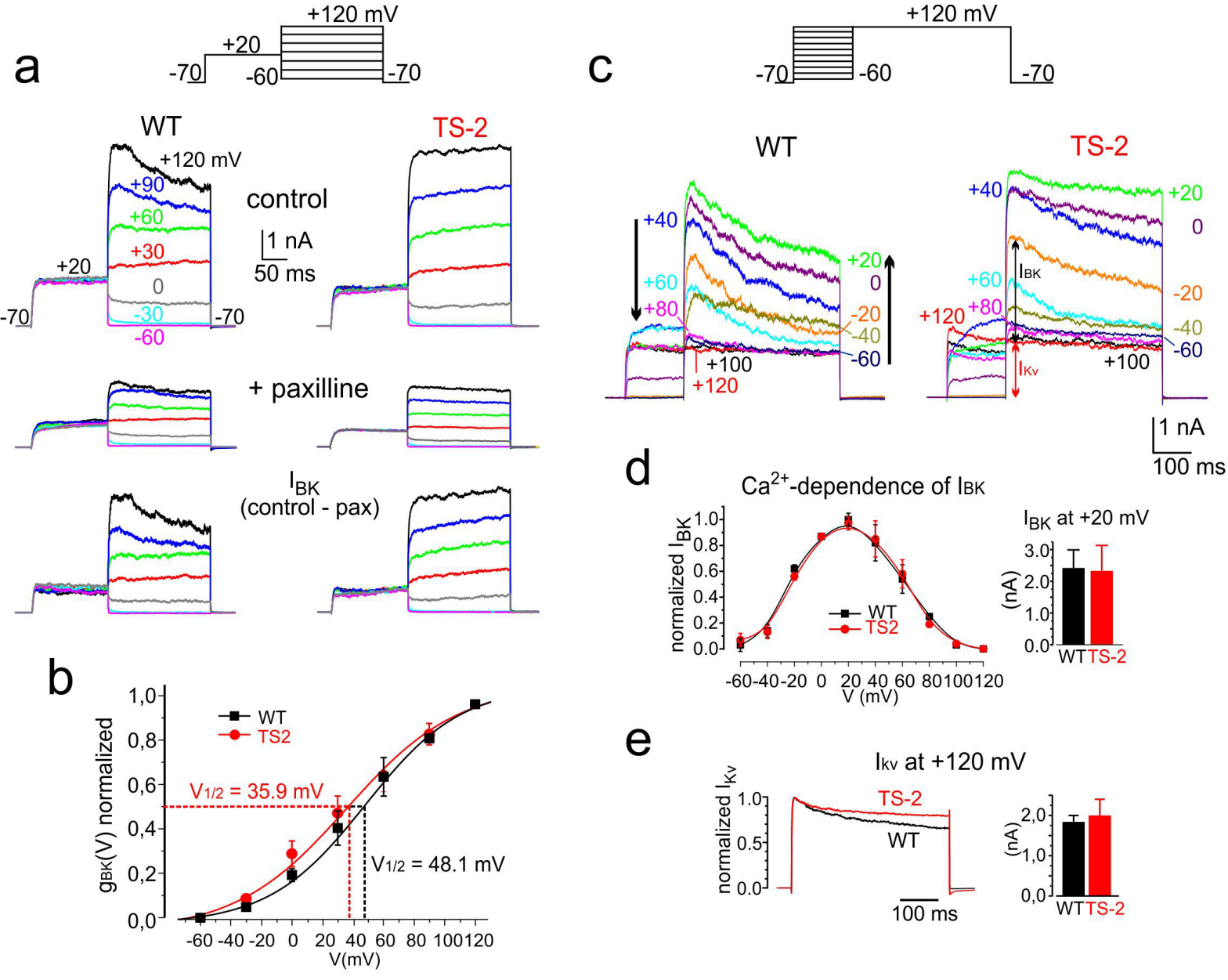
a
+120 mV
+20
-70
-60
-70
WT
TS-2
+120 mV
+90
+60
+30
0
-30
-60
+20
-70
-70
control
1 nA
50 ms
+ paxilline
IBK
(control - pax)
b
WT
TS2
gBK(V) normalized
V1/2 = 35.9 mV
V1/2 = 48.1 mV
V(mV)
c
+120 mV
-70
-60
-70
WT
TS-2
+40
+60
+80
+100
+120
+20
0
-20
-40
-60
IBK
IKv
1 nA
100 ms
d
Ca2+-dependence of IBK
normalized IBK
WT
TS2
V (mV)
IBK at +20 mV
(nA)
WT
TS-2
e
Ikv at +120 mV
normalized IKv
TS-2
WT
100 ms
(nA)
WT
TS-2

Fig. 9

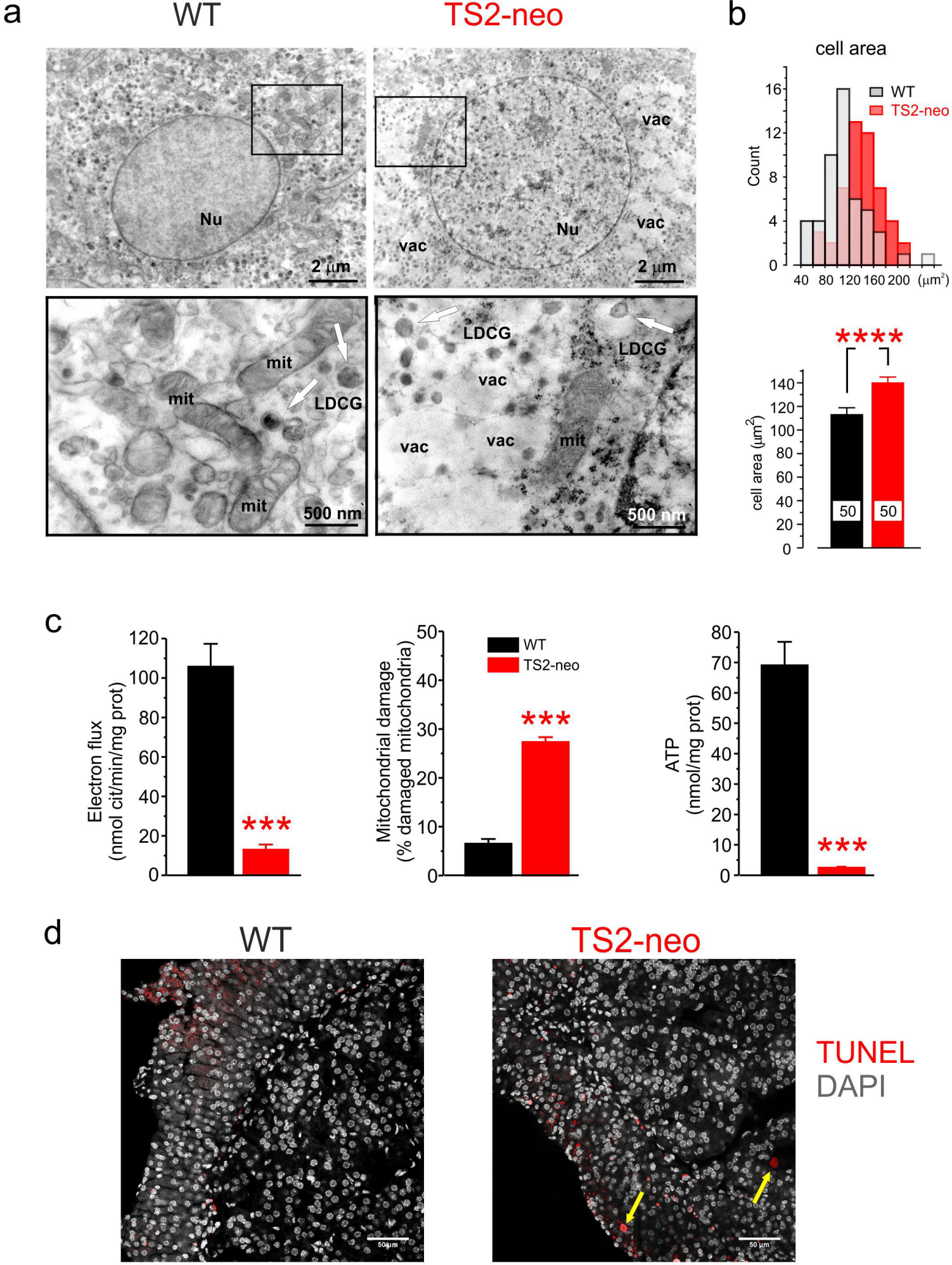
a
WT
TS2-neo
Nu
2 μm
vac
Nu
vac
vac
2 μm
mit
mit
LDCG
mit
500 nm
LDCG
LDCG
vac
vac
vac
mit
500 nm
b
cell area
WT
TS2-neo
Count
16
12
8
4
0
40 80 120 160 200 (μm²)
****
cell area (μm²)
140
120
100
80
60
40
20
0
50
50
c
Electron flux
(nmol cit/min/mg prot)
120
100
80
60
40
20
0
***
Mitochondrial damage
(% damaged mitochondria)
50
40
30
20
10
0
WT
TS2-neo
***
ATP
(nmol/mg prot)
80
70
60
50
40
30
20
10
0
***
d
WT
TS2-neo
50μm
50 μm
TUNEL
DAPI

Fig. 10

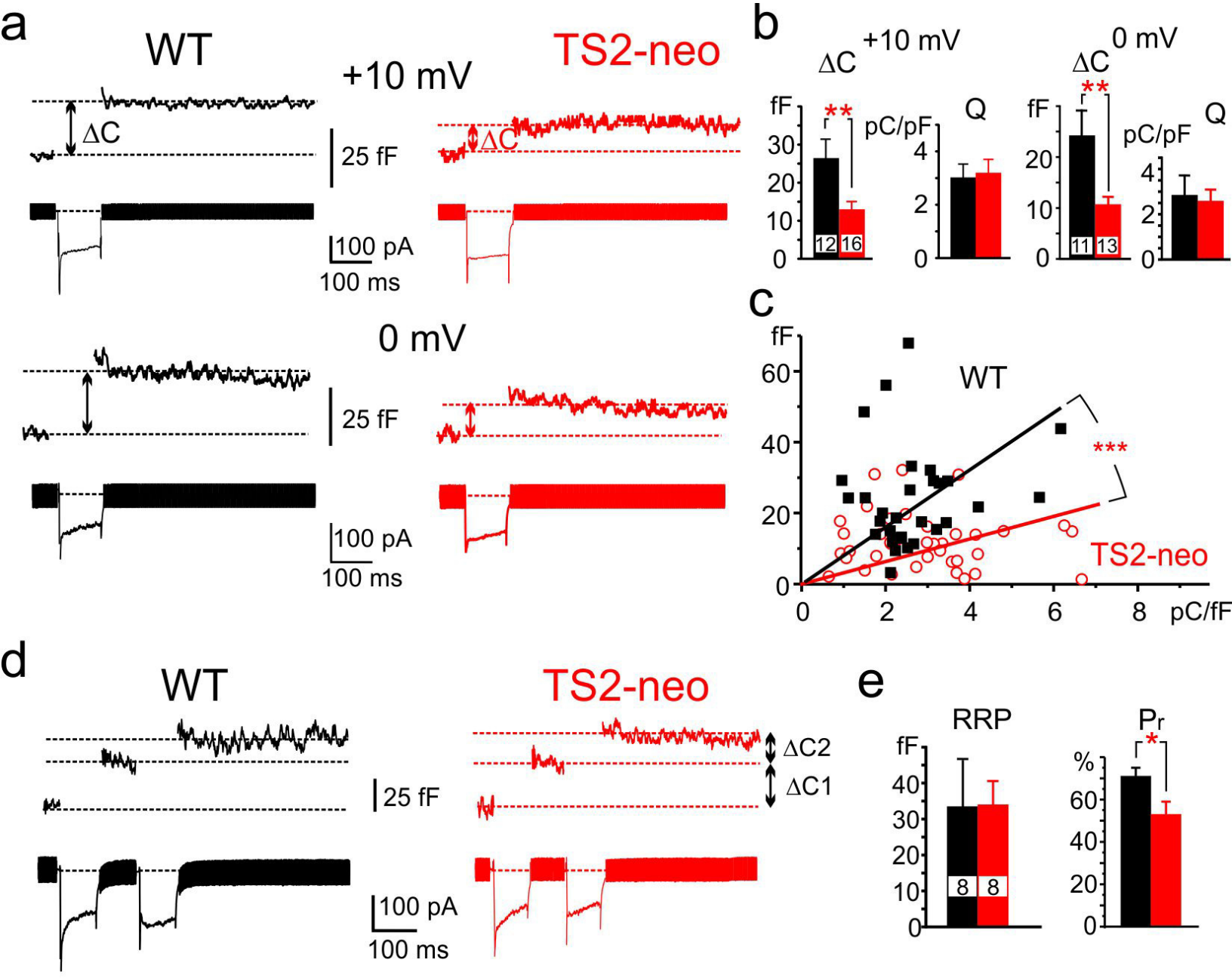
a
WT
TS2-neo
+10 mV
ΔC
25 fF
100 pA
100 ms
0 mV
b
+10 mV
0 mV
ΔC
fF
**
pC/pF
Q
12
16
11
13
c
WT
TS2-neo
***
fF
pC/fF
d
WT
TS2-neo
ΔC2
ΔC1
25 fF
100 pA
100 ms
e
RRP
Pr
fF
%
*
8
8

Fig. 11

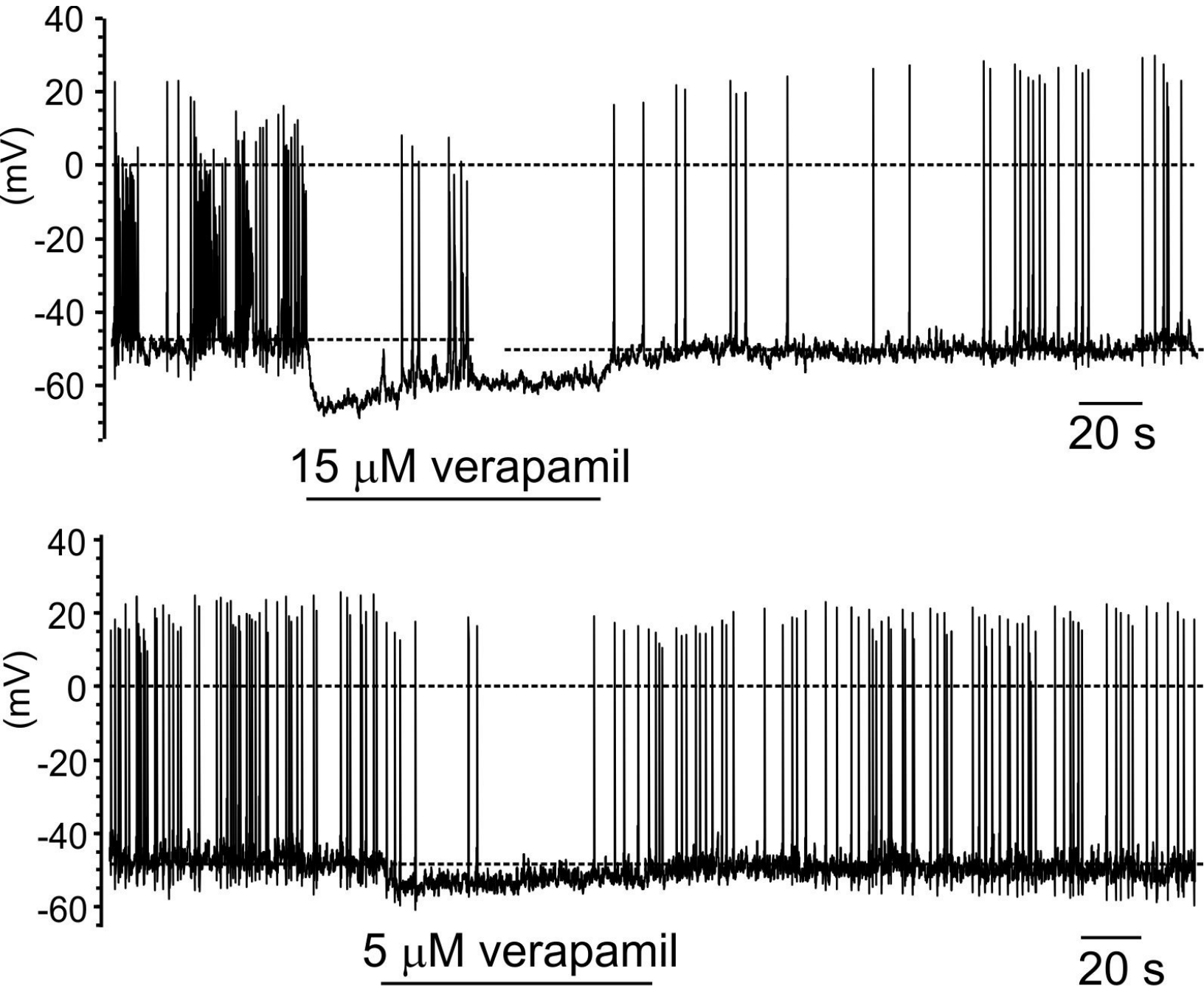
40
20
0
-20
-40
-60
(mV)
20 s
15 μM verapamil
40
20
0
-20
-40
-60
(mV)
5 μM verapamil
20 s

Fig. 12

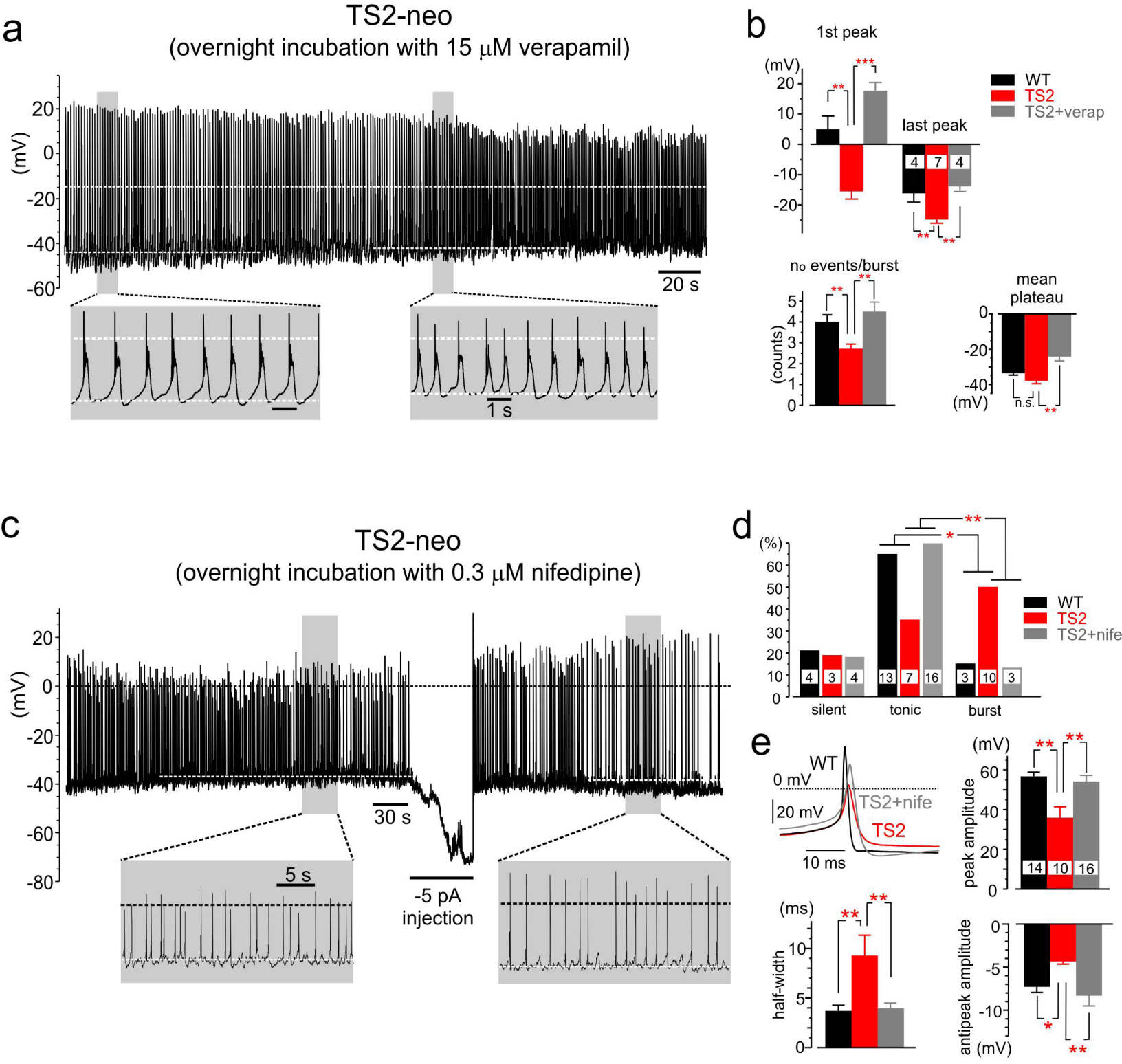
a
TS2-neo
(overnight incubation with 15 μM verapamil)
(mV)
20 s
1 s
b
1st peak
last peak
WT
TS2
TS2+verap
no events/burst
(counts)
mean plateau
(mV)
n.s.
c
TS2-neo
(overnight incubation with 0.3 μM nifedipine)
(mV)
30 s
5 s
-5 pA injection
d
(%)
WT
TS2
TS2+nife
silent
tonic
burst
e
WT
0 mV
20 mV
TS2+nife
TS2
10 ms
(ms)
half-width
peak amplitude
antipeak amplitude
(mV)

Fig. 13

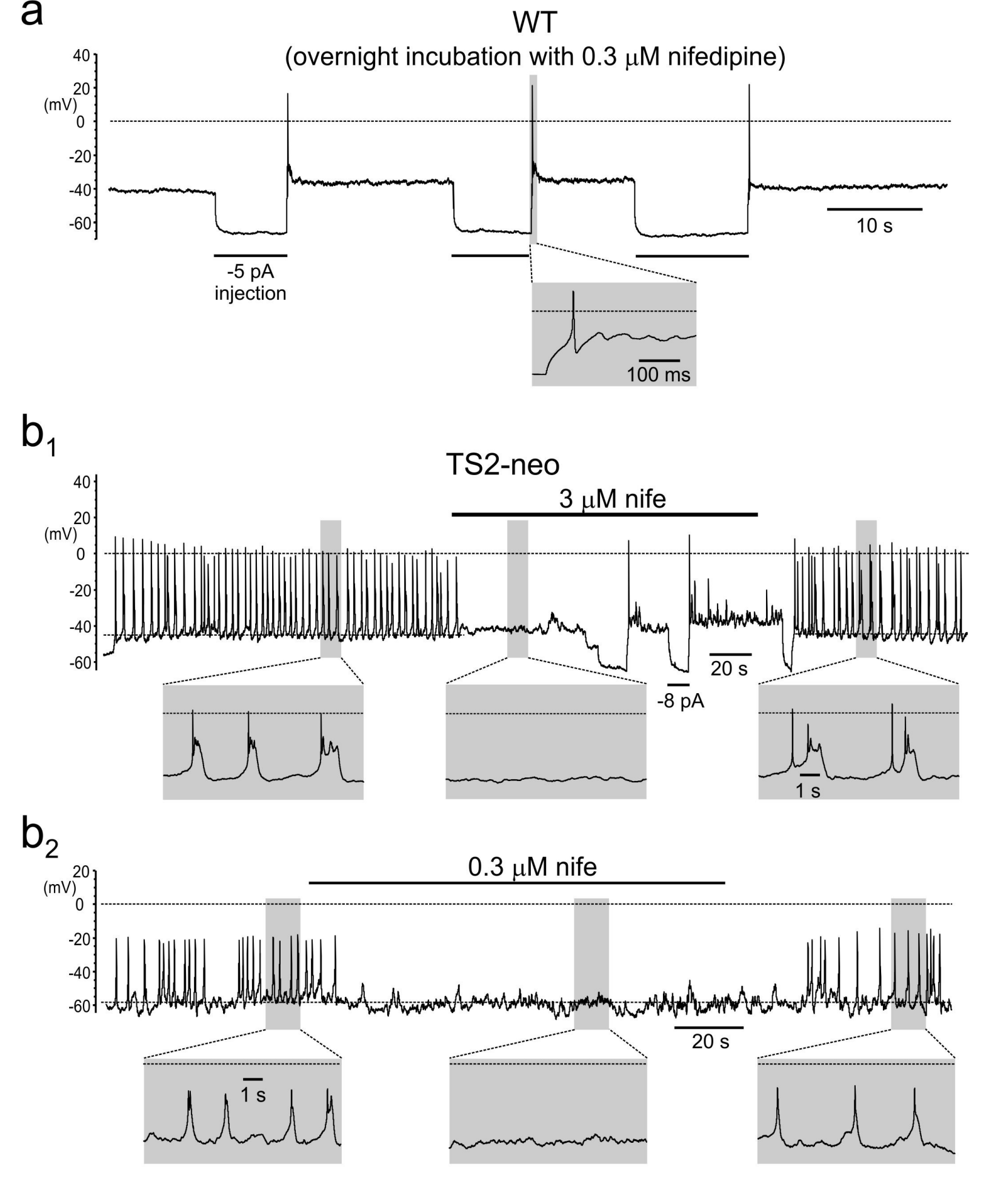
a
WT
(overnight incubation with 0.3 μM nifedipine)
40
20
(mV)
0
-20
-40
-60
10 s
-5 pA
injection
100 ms
b1
TS2-neo
3 μM nife
20 s
-8 pA
1 s
b2
0.3 μM nife
20 s
1 s

Fig. 14

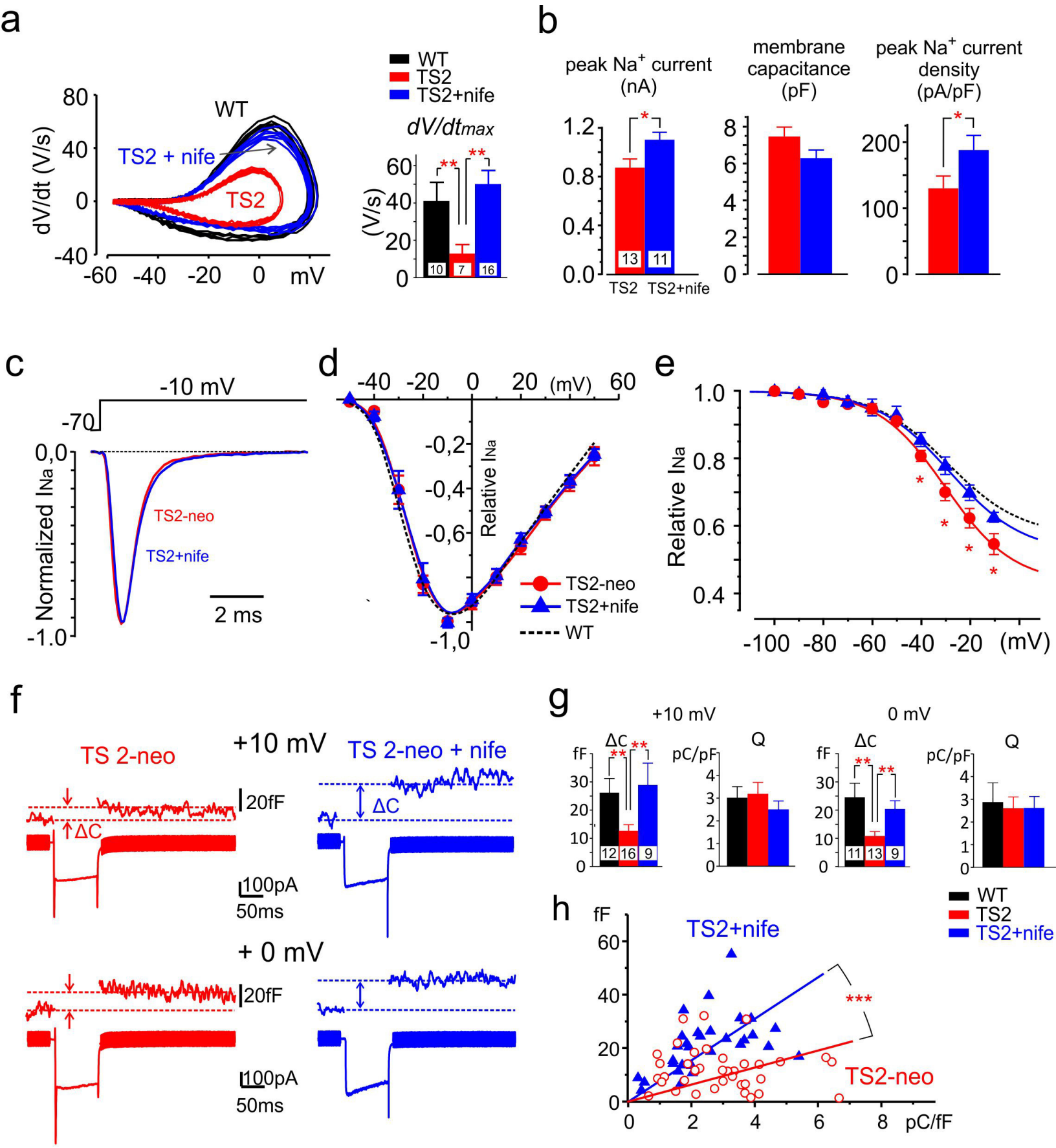
a
WT
TS2
TS2+nife
dV/dtmax
dV/dt (V/s)
TS2 + nife
TS2
mV
(V/s)
b
peak Na+ current (nA)
membrane capacitance (pF)
peak Na+ current density (pA/pF)
TS2
TS2+nife
c
-10 mV
-70
Normalized INa
TS2-neo
TS2+nife
2 ms
d
Relative INa
(mV)
TS2-neo
TS2+nife
WT
e
Relative INa
(mV)
f
TS 2-neo
+10 mV
TS 2-neo + nife
ΔC
20fF
100pA
50ms
+ 0 mV
g
+10 mV
0 mV
ΔC
Q
fF
pC/pF
WT
TS2
TS2+nife
h
fF
TS2+nife
TS2-neo
pC/fF

Fig.15